This is to certify that the
thesis entitled

THREE-DIMENSIONAL STRAIN ANALYSIS OF SINGLE-LAP BOLTED JOINTS IN THICK COMPOSITES USING FIBER-OPTIC STRAIN GAGES AND FINITE ELEMENT METHOD

presented by

GABRIEL A. ISAICU

has been accepted towards fulfillment
of the requirements for the

M.S. degree in Mechanical Engineering

Major Professor's Signature

3 August 2006

Date

THREE-DIMENSIONAL STRAIN ANALYSIS OF SINGLE-LAP BOLTED JOINTS IN THICK COMPOSITES USING FIBER-OPTIC STRAIN GAGES AND FINITE ELEMENT METHOD

By

Gabriel A. Isaicu

A THESIS

Submitted to
Michigan State University
in partial fulfillment of the requirements
for the degree of

MASTER OF SCIENCE

Department of Mechanical Engineering

2006

ABSTRACT

THREE-DIMENSIONAL STRAIN ANALYSIS OF SINGLE-LAP BOLTED JOINTS IN THICK COMPOSITES USING FIBER-OPTIC STRAIN GAGES AND FINITE ELEMENT METHOD

By

Gabriel A. Isaicu

Bolted joints involving composite plates used to be almost entirely dedicated to aero-space applications. As the need for energy conservation increases, the field of composite bolted joints finds new application in ground armored vehicles. Thick panels able to withstand large in-plane and impact loads are critical. This study was concerned with the evaluation of strain fields in thick composite plates used in single-lap bolted joints. The area of interest was the bearing plane region close to the bolt hole. Both experimental and finite element analyses were performed to evaluate possible failure causes and three-dimensional effects present in thick composite bolted joints. Experiments were performed for pin connection and bolted joint configurations. Experimental data for the pin connection and the bolted joints were recorded by embedded fiber-optic strain gages. The fiber-optic strain gages were embedded in the bearing plane of the composite plate. The numerical analysis was performed using both ANSYS and LS-DYNA finite element codes. The finite element analysis correlated reasonably well with the experiments.

to my beloved parents, Ligia and Aurel Isaicu

ACKNOWLEDGEMENTS

I would like to gratefully acknowledge Professor Gary L. Cloud for his continuous and determined support, sound advice and the opportunity to work on this project. I would like thank Dr. Dahsin Liu and Farhang Pourboghrat for their interest in this research. I would also like to thank my colleague, Dr. Gaetano Restivo, for the help, advice and efforts during this project. Last but not least I would like to thank my brother, Adrian, and my wife, Dominique, for all their patience, love and support. To all of the above, THANK YOU!

TABLE OF CONTENTS

LIST OF TABLES

LIST OF FIGURES

Appendix 1

KEY TO SYMBOLS

E - Young's elasticity modulus

ν – Poisson ratio

v - Volume

V - Volume fraction

G - Shear modulus

T - Installation torque

K - torque coefficient

D - nominal bolt diameter

P - clamping load

ε - strain

σ - stress

Chapter 1

INTRODUCTION

"The field of composite materials is both old and new. Is old in the sense that most natural objects, including human body, plants, animals are composite. It is new in the sense that only since the early 1960s have engineers and scientists exploited seriously the vast potential of fabricated fibrous composite materials" (1998).

Fastening composite structures induces yet another problem in the search for a complete understanding of their behavior. The simplest methods to fasten composites are bolting, riveting and bonding. Bonding and riveting do not allow for easy removal or replacement of damaged parts and inspection under limited-space conditions. Bolting composites, however, proves to be a very inexpensive and efficient solution. Parts can be easily removed and replaced, and structural integrity can be evaluated with ease. A standard single-lap bolted joint is shown in Figure 1.1.

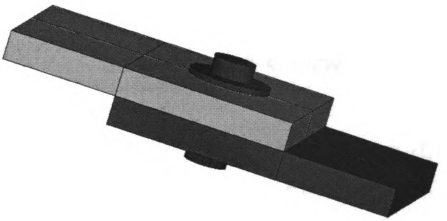

Figure 1.1 Single-lap bolted joint.

Many composite structures have been designed to be used in applications such as aerospace, ship building, sports equipment and circuit boards. These structures use mostly single or double-lap bolted joint configurations, and they are generally multi-fastened. Composite plates used for these applications are usually thin to moderately thick.

In the past few years, new applications that require increased strength are driving composite structures into new and innovative fields such as general automotive parts and ground armor transport vehicles. For these fields, a solid balance between strength and weight is needed. Strength is needed to safely replace current designs, and reduced weight is required for improved vehicle handling, fuel efficiency and, last but not least, fast deployment.

1.1 LITERATURE REVIEW

Past and present research dedicated to bolted joints of composite structures is channeled in two main directions: experimental studies on failure and damage propagation and, the newest trend, numerical simulations. Advances made in computing power in the past decade influenced the development of powerful computer programs capable of simulating mechanical interactions such as contact between three-dimensional surfaces and dynamic contact between mechanical components.

1.1.1 Purely Experimental Studies

To take advantage of Fiber Reinforced Polymers (FRP) composite structures, complete analyses of stress and strain distributions in the composite structure are needed. The influence of stress concentration factors such as the bolt hole, bolt hole to plate edge distance, hole diameter, and bolt-to-hole clearance have to be fully understood.

The most common types of failure in composite structures are shown in Figure 1.2.

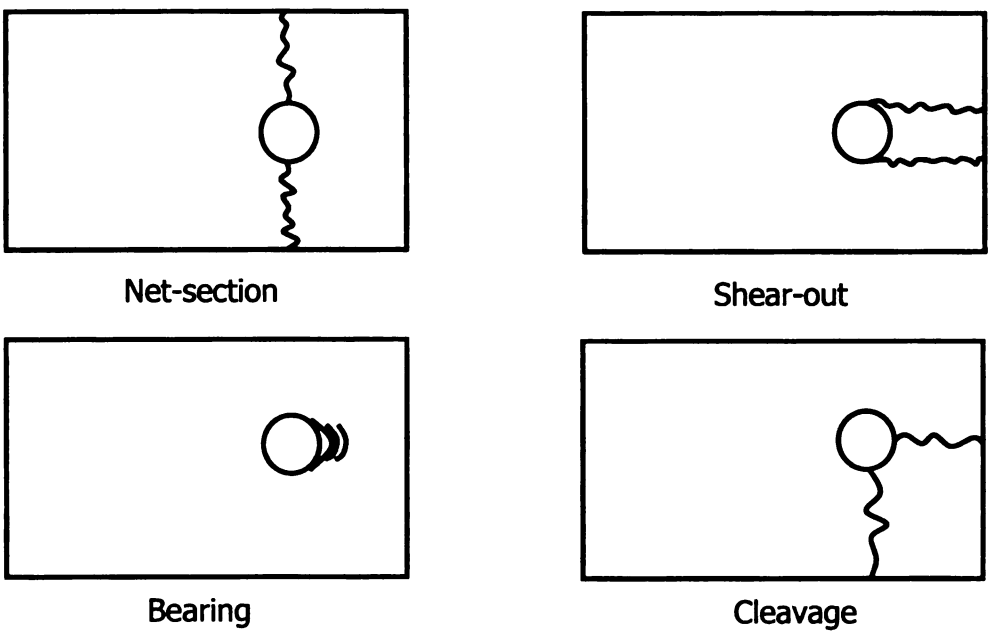

Figure 1.2 Basic failure modes.

Specific failure modes in FRP composites are shown in Figure 1.3.

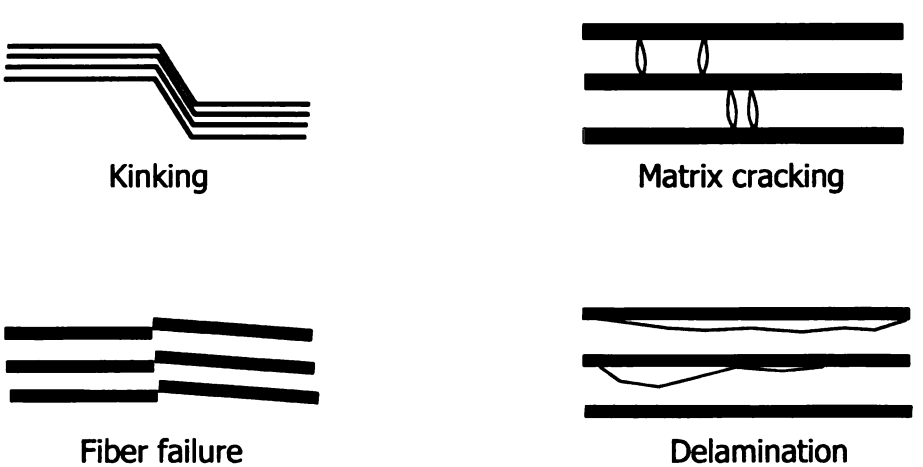

Figure 1.3 FRP specific failure modes.

In an extended experimental study on damage development in mechanically fastened laminate composites, Ireman *et al.* (2000) used graphite/epoxy laminates in an attempt to characterize damage development close to the bolt hole. The laminate configurations in test specimens were quasi-isotropic: $[(\pm 45/0/90)_4]_S$ and $[(\pm 45/0/90)_8]_S$; and zero-dominant $[(\pm 45/90/0_2/90/0_2)_2]_S$. The thicknesses of the composite plates used in this study were 4.16mm and 8.32mm, corresponding to 0.16in and 0.32in, respectively. The study used both single and multi-bolt configurations of single-lap joints in conjunction with a special fixture to eliminate the bending moment caused by the eccentric load path (secondary bending). Both countersunk and protruding head bolts were used. Damage development was assessed using resistance strain gages, acoustic emission, X-ray, and by microscopic examinations. Destructive examination was performed, as the specimens were cut and polished and then examined under the microscope. The specimens were loaded a number of times (six or seven) and monitored by acoustic emission. When acoustic emission showed that some damage occurred to the specimen, the loading was stopped and the specimen was examined by X-ray and microscope. The study concluded that the specimens tend to experience the whole palette of FRP failure modes before total failure is reached. As the load increases the specimens show matrix cracking, fiber failure, delamination and kinking followed by total failure.

Hou and Liu (2003) studied the effects of size and thickness on the composite joints. Glass/epoxy specimens with [0,90] stacking sequence of 9, 17 and 34 plies were employed in a double-lap pin joint configuration. Specimens were 0.13in, 0.25in and 0.5in thick. On the effect of joint length on the composite joint, the study concluded that as the ratio between the length from the hole to the clamped end over the width passed 4, the joint strength remains fairly constant. Investigations of three-dimensional size effects revealed that the ratio of thickness over the hole diameter was found to be a critical value for the composite joint. The effect of pin-hole clearance values over the joint was clear, with the joint strength decreasing as the clearance increased. As the loading rate increased, an increase in the joint strength was observed. The study also concluded that as the FRP plate thickness increased, a decrease in strength was observed. This result was compared to the Weibull theory. All specimens except the one with 34 plies and 0.5in thickness experienced bearing damage. The 0.5in thick specimen experienced total net-section failure.

Lawlor, McCarthy and Stanley (2002) did an experimental study concerned with the effects of clearance on single-lap single-bolt composite joints. The specimens were made of carbon fiber/epoxy with the thickness between 0.11in and 0.2in having two different stacking sequences: one quasi-isotropic and one zero-dominated. Bolts used were aerospace grade titanium alloy with 8mm (0.31in) nominal diameter. Both protruding head and countersunk fasteners were

used along with steel washers and nuts. The bolt torques applied were "finger tight" and 141 lb-in. Clearance was obtained by using constant nominal diameter bolts and by varying hole diameter. The study concludes that the main effects of clearance were concentrated in stiffness and ultimate strain variation with little effect on strength. An expected delay in load take-up and better load distribution were experienced with high clearance value specimens.

An experimental study on fatigue resistance of composite joints using protruding head bolts, written by Starikov and Schon (2002), employed carbon fiber/epoxy plates with quasi-isotropic and 0-degree lay-ups. Specimens were used in single and double-lap multi-bolt configurations. All specimens had the same thickness of 3.12mm (0.12in). Bolts used in this study were titanium with protruding heads (hexagon type). The single-lap configuration used 6 bolts evenly distributed in 3 lines. Bolts were tightened with 80lb-in torque. Fatigue tests were performed by loading and unloading the specimen. The number of cycles used was in the range 10^3-10^6, depending on when failure of the bolted joint occurred. Measurements were done using resistance strain gages to analyze strain distribution and load transfer between bolt rows. Extensometers were used to evaluate relative displacement between composite plates. The plates were loaded using two approaches: additional plates glued to the specimen or lateral supports with Teflon lubrication. Both approaches are used to avoid secondary bending. The study concluded that there is a linear dependence between the

fatigue resistance and the number of bolts used in the joint. Bolt failure was the dominant cause of joint failure. However, the joints supporting the highest loads failed in two modes.

Tong (2000) studied the bearing failure of composite bolted joints with non-uniform bolt-to-washer clearance. The study focused on the relative positions of the bolt and washer on the bearing failure of the bolted joint. Composite plates were made of carbon/epoxy using a quasi-isotropic stacking sequence. The specimens were set to have 8 plies of plain carbon weave adding up to 1.72mm (0.068in) in thickness. Steel bolts, nuts and washers were used for the joining of the composite panel to two steel plates in a double lap configuration. A piezoelectric load cell transducer was used to measure clamping loads. Experimental results were compared to analytical results based on a modified model of Herrington and Sabbaghian. The author observed good agreement for the case when the washer is offset in the loading direction and poor agreement for the case when the washer is offset opposite to the loading direction. Possible causes that may influence the agreement between experimental and analytical results are listed. The study concludes that the extreme positions of the washer to the bolt shank slightly affects the initial failure load but has no significant influence on the ultimate failure load.

Herrera-Franco and Cloud (1992) did an experimental study concerning the stress and strain distributions in the vicinity of single-pin lap joints. The study presented options for reducing stress concentrations by use of hole inserts. The specimens used were made of thirteen layers of regular symmetric cross-ply glass/epoxy having a 0.14in thickness. The specimens were loaded in a double-lap single-bolt configuration. Measurements of surface stress and strain fields in the neighborhood of the hole were performed by means of moiré interferometry. Measurements were taken for no insert, a hard insert (aluminum) and a soft insert (epoxy) in an isotropic material and in the glass/epoxy composite. High sensitivity moiré interferometery was used to measure surface strains within the insert ring. One of the conclusions reached by the authors was that a 50% reduction in bearing strains for the case of a soft insert ring, compared with the no-insert case in the composite plate. Also, approximately 50% reduction of the shear strain in the bearing region is observed. For the case of the hard insert, there was a 90% reduction of the bearing stress at the edge of the hole compared to the no-insert case.

1.1.2 Combined Experimental and Finite Element Analysis Studies

Previous finite element models built to simulate bolted joints were mainly conducted only two-dimensional analyses. Few of the studies conducted with the

help of the Finite Element Analysis (FEA) modeled the bolted joint as a three-dimensional model.

One of first studies concerned with three-dimensional stress analysis of a composite laminate bolted joint was developed by Chen, Lee and Yah (1995). The study reports on a general method of evaluating contact stresses generated by the bolt-hole interaction using an incremental variational principle formulation and the transformation matrix derived from three-dimensional contact kinematic conditions. The numerical results obtained were compared with experimental results from a double-lap bolted joint. The composite plates used in the experiment were thin graphite/epoxy with $[\pm 45/0/90]_S$ quasi-isotropic lay-up and thick glass/epoxy of various stacking sequences. The effects of friction, clearance, bolt elasticity, stacking sequence and clamping on the contact tractions around the bolted joint were included in the analysis. Clamping force was modeled as pressure and it was determined analytically. Good agreement between the numerical results and the referenced experimental results was reported.

Another study by Chutima and Blackie (1996) looked into the effects of pitch distance, row spacing, end distance and bolt diameter on multi-fastened composite joints. The authors limited their study to a multi-bolt double-lap configuration of the bolted joint. The study used a two-dimensional finite

element model to calculate contact stresses and load distribution. The study reported that friction at the bolt-hole interface exerted a considerable effect on the local contact stress distribution around the holes.

Camanho and Matthews (1997) wrote a review of the investigations that have been made on the stress and strength analysis of bolted joints in FRP composites. The review highlighted different methods used to predict failure in single or multi-fastener joints, numerical approaches that include two and three-dimensional models as well as an assessment of the effects of clearance, friction and geometry. The authors concluded that in order to include important aspects of the joint's behavior and strength the use of three-dimensional models is necessary.

Ireman (1998) did a three-dimensional stress analysis of bolted single-lap composite joints. A three-dimensional finite element model of the composite bolted joint was developed to determine non-uniform stress distributions through the thickness of composite laminates in the proximity of the bolt hole. The finite element models were created using IDEAS and solved using ABAQUS, a commercially available finite element software. Added supports were used to eliminate secondary bending due to offset boundary conditions. One coefficient of friction was used for all contact surfaces due to software limitations. Numerical results were compared against strain gage measurements.

Kermanidis *et al.* (2000) developed a three-dimensional progressive damage model to simulate damage accumulation in single-lap bolted joints. Stress analysis was performed using ANSYS software and the model was incorporated in the ANSYS solving routine. The model was based on the Hashin-type criteria and contained a set of degradation rules. FEA results were then compared to experimental results from Ireman's study (1998).

Whitney *et al.* (2004) studied singular stress fields near contact boundaries in composite bolted joints. The study focused on the singular stresses arising in the vicinity of contact surfaces induced in laminated orthotropic plates by mechanical fastening. The investigations were done using local asymptotic solutions and full-field numerical analysis. Frictionless contact conditions were assumed. The bolted joint numerical model considered symmetry with respect to the contact plane between the two plates forming the bolted joint.

A study conducted by Iancu *et al.* (2004) studied bolted joints of an isotropic material and aluminum. A three-dimensional numerical model was built and results were compared against photoelasticity and resistance strain gages (RSG) experimental results. The model boundary conditions were such that secondary bending was eliminated. Good agreement between experimental and numerical results was reported.

Chapter 2

RESEARCH OBJECTIVES

As mentioned in Chapter 1, most of the past studies concentrated on two-dimensional finite element numerical models, and just a few studies approached the three-dimensional finite element numerical models. From the three-dimensional finite element models one can observe that most of them are concerned with either double-lap bolted joints or single-lap bolted joints modified such that the bending caused by the eccentric loading path is not included in the analysis.

Previous studies contained experimental data from resistance strain gages applied on the surface of the composite plate. This approach does not allow measurements very close to the bolt hole, nor on the bearing plane of the specimen. One study included resistance strain gages inside an isotropic specimen with fairly good results. Using resistance strain gages inside a laminate composite plate would not be desirable because it could alter the mechanical properties of the composite plate in a significant manner.

Since "traditional applications" of laminate composite materials have mostly been concentrated in the aerospace and electronics related fields, composite plates generally have low thickness value. The importance of such applications led researchers into studying thin composite plates. But, as omposite engineering evolves and more and more fields require the balance between strength and weight that the laminate composites offer, more investigations are necessary to characterize the behavior of thicker, more complex composite materials.

This research studied a single-lap bolted joint between a thick laminate composite plate and an aluminum plate. The bolted joint was modeled numerically using finite element analysis and it included the fastening parts: washers, nut and bolt. The numerical results were then compared with experimental data coming from fiber-optic strain gages (FoSG) embedded in the thick composite plate. Since most of the damage supported by the laminate is bearing damage, as shown in Figure 1.2, this analysis concentrated on measurements in the bearing plane of the laminate composite plate. The position and magnitude of the stress and strains in the specimen were reported.

The finite element analysis provides a complete three-dimensional map of stresses and strains. The experimental data obtained through the thickness of the composite plate provides valuable information from within the specimen. The

investigations were done on glass reinforced epoxy plates. Future studies will be concentrated on very thick sandwich composite materials.

The methods used in this research were chosen based on some very important factors. The finite element analysis is able to provide three-dimensional data map that is practically impossible to obtain with a reasonable number of sensors. Finite element analysis proves to be a very inexpensive tool in the study of fiber reinforced composite materials. With all the advantages of the finite element method, the numerical model has to be first tested so that accuracy of results can be evaluated. Improvements to the model are then possible so that the numerical model can be used with confidence to obtain qualitative as well as quantitative results.

Fiber-optic strain gages were chosen for their miniscule dimensions without jeopardizing accuracy. These sensors can be embedded in the specimen at the time of fabrication and they do not significantly affect the material properties of the thick composite laminate plate. The data stream coming from the sensors can be used at any given time for validation purposes, as well as for health monitoring of the composite joint during its service life.

From here on, this thesis is structured as follows: Chapter 3 deals with experimental setup, specimen characteristics and composite material property

validation. Chapter 4 presents the main points of the finite element model and will present reasons why certain settings were chosen. Chapter 5 gives an overview of the results obtained and results comparison. Chapter 6 provides conclusions drawn from this study. Chapter 7 focuses on possible error causes and suggestions.

The most challenging part of the finite element analysis is modeling the contact involved in the bolted joint. This task proves to have a large influence on the numerical results and it needs to be carefully addressed. Another crucial factor is correct determination of the clamping force for bolted joints. Also, material properties have to be correctly determined, such that the input parameters of the finite element model are in accordance with the experiment. The details on the modeling of the contact surfaces is included in Chapter 4. Details about the determination of the clamping load and material properties calibration, as well as the studied load cases, are covered in Chapter 3.

Chapter 3

EXPERIMENTAL ANALYSIS

Experimental analysis for this research is a means of validating the finite element analysis that gives valuable insight into the strain and stress distributions in thick laminate composite plates in single-lap bolted joints.

The method of choice for experimental investigations was using fiber-optic strain gages. The fiber-optic sensors were used to measure strains inside the composite plate, in the bearing plane. These readings were not sufficient for the finite element analysis and other experiments were done to gather the necessary data for input into the finite element model. Material properties and clamping force were important parameters that needed to be accurately determined.

Experimental investigations for material properties validation and some of the bolted joint experiments were done in collaboration with Xu Ding and Gaetano Restivo, as part of the comprehensive research program.

3.1 FIBER-OPTIC STRAIN GAGES

A brief outlook over the theory behind fiber-optic sensors, with accent on the fiber-optic strain sensors, is necessary for understanding the use and usefulness of these new-generation sensors.

What is a sensor? A sensor is any a device which converts a physical property of interest into a different form of energy which can be transmitted, processed and correlated to the physical property. In our case, the sensor is a Fabry-Perot cavity and the form of energy that transmits the signal is an optical signal.

The medium that carries the signal to and from the sensor is the optical fiber. The optical fiber is made of a very thin silica core surrounded by a silica cladding that has a lower refractive index than the core. The obtained effect is that the light is guided through the core from the source to the other end of the optical fiber as it can be seen in Figure 3.1. The core and the cladding are then protected by a silicon coating followed by buffer jacket, strength members and outer polyurethane jacket. These protection coatings can differ depending on the application.

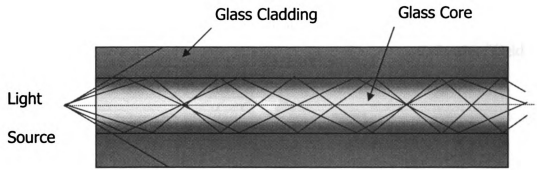

Figure 3.1 Light paths through generic optical fiber.

The Fabry-Perot sensor consists of two partially reflective mirrors separated by a cavity. In the intrinsic form, the mirrors are fabricated within the fiber, thus the cavity is actually the fiber itself. In the extrinsic version of the Fabry-Perot sensors, as shown in Figure 3.2, the two mirrors are separated by an air gap. The light traveling through the fiber is partially reflected back by the first mirror. The remaining light enters the cavity and is reflected back and forth between the mirrors. Interference occurs between the light beams resulting in a phase shift due to the additional optical path.

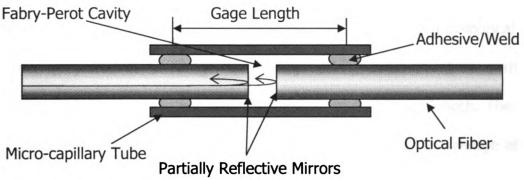

Figure 3.2 Typical Fabry-Perot strain sensor.

The interrogator, patented by Bellville and Duplain (1993; 1995) is based on a white-light Fizeau interferometer shown in Figure 3.3.

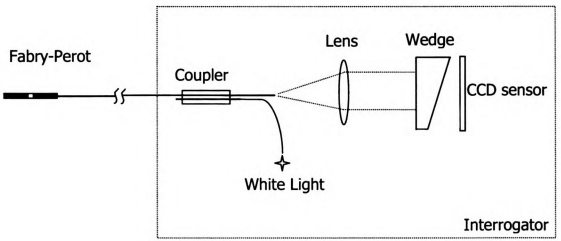

Figure 3.3 Typical Extrinsic Fabry-Perot Deployment.

The light from a broadband source is sent along one of the fiber branches. It arrives in the coupler where it is transmitted along the fiber branch bearing

the sensor. The light is bounced by the two mirrors and reflected back to the signal conditioner. The modulated light is then passed through a cylindrical lens and then projected on a wedge. The wedge acts a cross-correlator with the position of the light on the wedge as a function of the cavity length. The light corresponding to d μm of cavity length will be projected on the wedge at the point where the wedge thickness is d μm. Cross-correlation is obtained instantaneously by passing the light through the glass wedge. The light then falls on a linear CCD array for which each pixel corresponds to a specific correlated cavity length (1993).

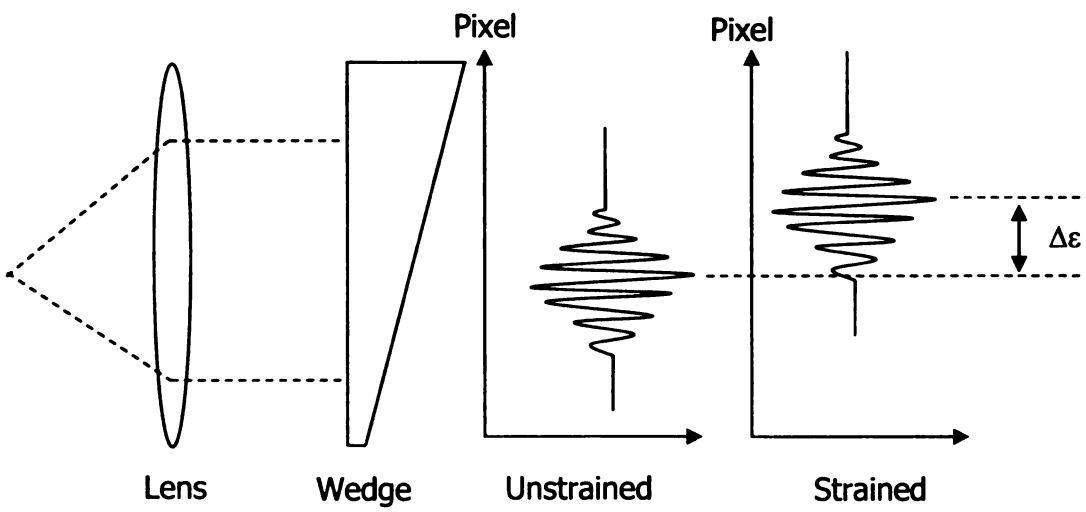

Figure 3.4 Cross correlation using Fizeau interferometer.

Some of the advantages fiber-optic sensors offer are: small size, easy embedment, low transverse load sensitivity, small gage length, EMI/RFI

interference immunity, ability to implement in hostile environments without fearing corrosion and mechanical strength, to name a few.

For the purpose of this research, fiber-optic sensors brought a novel approach for the characterization of strain fields inside the laminate material. As mentioned before, most of the research done in this field used surface mounted resistance strain gages to validate numerical models. By embedding even miniscule foil gages into laminate specimens, the material properties of the laminate would most likely suffer alterations that affect the experiment.

All fiber-optic strain gages used in this research are non-compensated type gages having a 2mm gage length as manufactured by FISO Technologies. The outer diameter of the strain gage is 230μm. Schematics of the fiber-optic gage used in this research is shown in Figure 3.5.

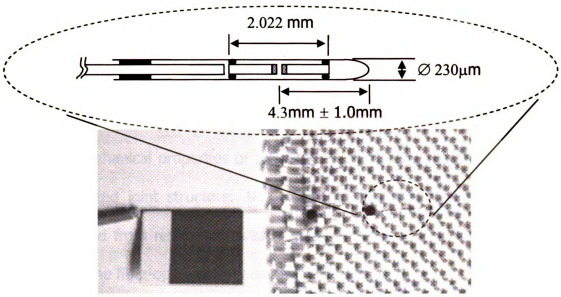

Figure 3.5 Fiber-optic strain gage (FOSG) glued to the E-glass weave with schematics of the FOSG.

3.2 MATERIAL PROPERTIES VALIDATION

The objective of this part of the research work was validation of two important mechanical properties of the laminate composite material used in the single-lap bolted joint structure. Also, by comparing the measured results of strain obtained from resistance strain gages and fiber-optic strain sensors, the efficiency of the fiber-optic sensors can be evaluated.

To be consistent with proceeding research work, Epoxies, Etc... 20-3302 epoxy resin and E-glass fiber weave were used. Epoxies, Etc... 20-3302 is a two-component, ultra-clear, epoxy system designed for L.E.D. (Light Emitting Diode) encapsulation, fiber optics, and any potting or adhesive application requiring optimum clarity. Material properties are shown in Table 3.1.

E-glass fiber	E (PSI)	10.5e6	ν	0.22
Epoxy	E (PSI)	0.5e6	ν	0.37

Table 3.1 E-glass and epoxy resin properties

In order to obtain the desired thickness of 0.5in, 60 plies of E-glass weave were used for each specimen. The plain weave had 18warp/in and 18fill/in fiber counts.

3.2.1 Volume Fraction Determination

Volume fraction determination was needed to determine the macro-mechanical material properties of the composite plate. Since macro-mechanical properties were to be used in the finite element analysis, an accurate determination was necessary.

Volume fraction calculations were performed on one of the first specimens used in this research study. The same materials were used for all specimens included in the study thus the change in volume fraction, from one specimen to another, was considered to be negligible. Dimensions of the specimen used for determining the volume fraction are 4.35inx3.91inx0.5in (Length x Width x Height). The specimen had 60 plies of plain weave style 3733.

The volume of the plate can be expressed in terms of the volumes occupied by the fiber and the matrix. The void content of the plate is assumed to be negligible at this time.

$$v_{plate} = v_{fiber} + v_{matrix} \qquad 3.1$$

Dividing the above equation by the plate volume , we obtain the volume fraction relationship:

$$1 = \frac{v_{fiber}}{v_{plate}} + \frac{v_{matrix}}{v_{plate}} = V_{fiber} + V_{matrix} \qquad 3.2$$

The plate volume was calculated based on the plate dimensions and it was found to be v_{plate}= 8.50in.

The weight of the plain weave was recorded for a stack of 60 plies and it was found to be 4.466oz. The density of E-glass fiber is 0.093 lbm/in^3 (1998). Thus, the volume occupied by the fibers is v_{plate}=3.00in^3. Dividing the volume occupied by the fibers by the total volume of the plate, the volume fraction of the specimen is V_{fiber}=0.35.

3.2.2 Experimental Validation of Material Properties

The finite element model can use layered elements to represent the stacking of E-glass fibers and epoxy. Then it can use a homogenization scheme to calculate the effective material properties for the laminate plate. This step was avoided due to heavy calculation volume. It is also an error-prone scheme due to the fact that fiber lay-up is not a pure $[0/90]_s$ because of undulations of the woven fibers.

Material properties were then acquired from a model by Dasgupta *et al.* (1996). This model accounted for the undulations in the weave and it provided the necessary data to determine homogenized mechanical properties of the laminate as a whole. The determined orthotropic material properties were then included into the finite element numerical model. Material properties of the laminate are shown in Table 3.2.

Component	E_x **(psi)**	E_y **(psi)**	E_z **(psi)**	ν_{xy}	$\nu_{xz}=\nu_{yz}$	G_{xy} **(psi)**	$G_{xz}=G_{yz}$ **(psi)**
Composite plate	2.46e6	2.46e6	4.78e5	0.38	0.14	4.2e5	2.72e5

Table 3.2 Composite laminate material properties.

The advantages of using orthotropic material properties for the finite element numerical models are not insignificant. Calculation time is greatly reduced because of the use of lower order elements having a lower number of degrees of freedom (DOFs). Convergence problems are also avoided due to the simplified model.

After the determination of the material properties of the laminate, validation of the material properties was necessary to prove the accuracy of the determinations and to provide a solid base for the numerical model. For

validation, a specimen having the same lay-up scheme and volume fraction was used in a tensile test.

For the tensile test, a combination of Micro-Measurements EA-13-120LZ-120 0-90° resistance strain gage rosettes and FISO fiber-optic strain gages was used. By using both methods, the conventional and well known resistance strain gages and the new generation of sensors, the fiber-optic strain sensors, a validation of the fiber-optic sensors was possible.

Two fiber-optic sensors were attached to the 30th E-glass layer prior to specimen fabrication. Attachment of the sensors to the weave is necessary in order to preserve the sensor's position during fabrication. Sensor repositioning would be impossible after the epoxy cures. Two small blobs of Devcon Aluminum Liquid (F-2) metal-filled epoxy secured the naked fiber to the weave. The metal filled epoxy would be an advantage for X-ray localization of multiple fiber-optic strain gages.

A sample attachment of a fiber optic sensor to the E-glass weave can be seen in Figure 3.6. The portion of the fiber where the strain gage is located is not glued at this point. During fabrication the epoxy secures the sensor within two consecutive layers of E-glass weave.

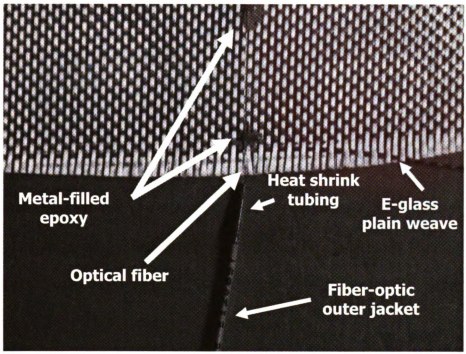

Figure 3.6 Sample attachment of fiber-optic strain gages to E-glass weave.

A microscopic view of a fiber-optic strain gage attachment point is shown in Figure 3.7.

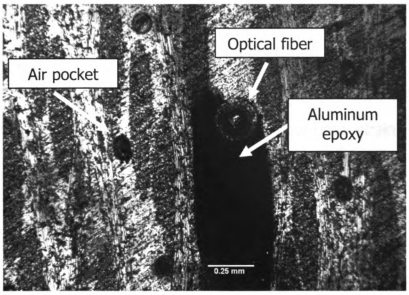

Figure 3.7 Optical fiber attachment point.

The two 0-90° resistance strain gage rosettes were attached to opposite faces of the specimen. The rosettes provided valuable data for avoiding bending during testing and material properties validation. The tensile test specimen, as shown in Figure 3.8, was 10in long, 2.25in wide and 0.5in thick.

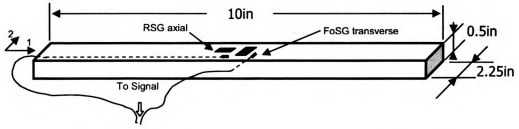

Figure 3.8 Tensile test specimen and strain gage layout.

The tensile test specimen was set up in the load frame as seen in Figure 3.9. The RSGs were connected to Measurements Group P-3500 Strain Indicator setups in half-bridge configuration with temperature compensation gages mounted on an unloaded specimen. The FISO fiber-optic strain gages were connected to an 8-channel FISO UMI-8 signal conditioner that provided a data stream to a portable laptop computer.

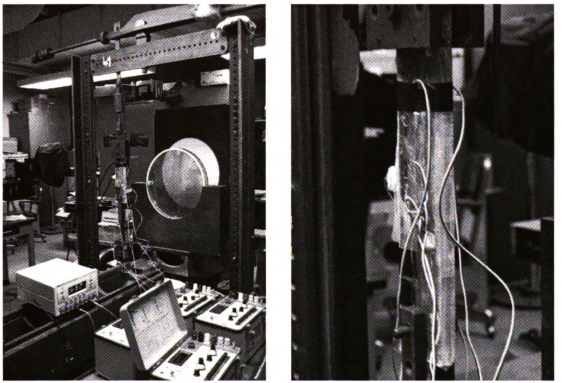

Figure 3.9 Tensile test loading setup and data acquisition equipment.

To minimize any effect of bending caused by misalignment of loading fixture, the loading setup was adjusted until matching readings were obtained from the two RSG rosettes within 10% variation. The tensile specimen was

loaded from 0 to 200 lbs. Readings were taken at 5 minutes after each loading. Strain readings are shown in Table 3.3.

Load(Lb)	Stress(PSI)	Axial RSG (με)	Transverse RSG (με)	Axial FOS (με)	Transverse FOS (με)
25	21.7	8	-2	8	-0.5
50	43.4	17	-3	16	-1.5
75	65.2	25	-4	24	-2.5
100	86.94	34	-5	33.5	-3
125	108.6	42	-7	41.5	-4
150	130.4	52	-8	51	-5.5
175	152.1	60.5	-9	59	-6
200	173.9	70	-10	68.5	-6.5

Table 3.3 Readings from the RSG rosettes and fiber-optic strain gages.

In parallel with the experiment, a finite element model numerical analysis was performed. The numerical model of the tensile specimen with analytically calculated material properties was simulated under the same load conditions as in the experiment. A comparison between the finite element numerical results, results from the fiber-optic strain gages and from RSG rosettes is shown in Figure 3.10.

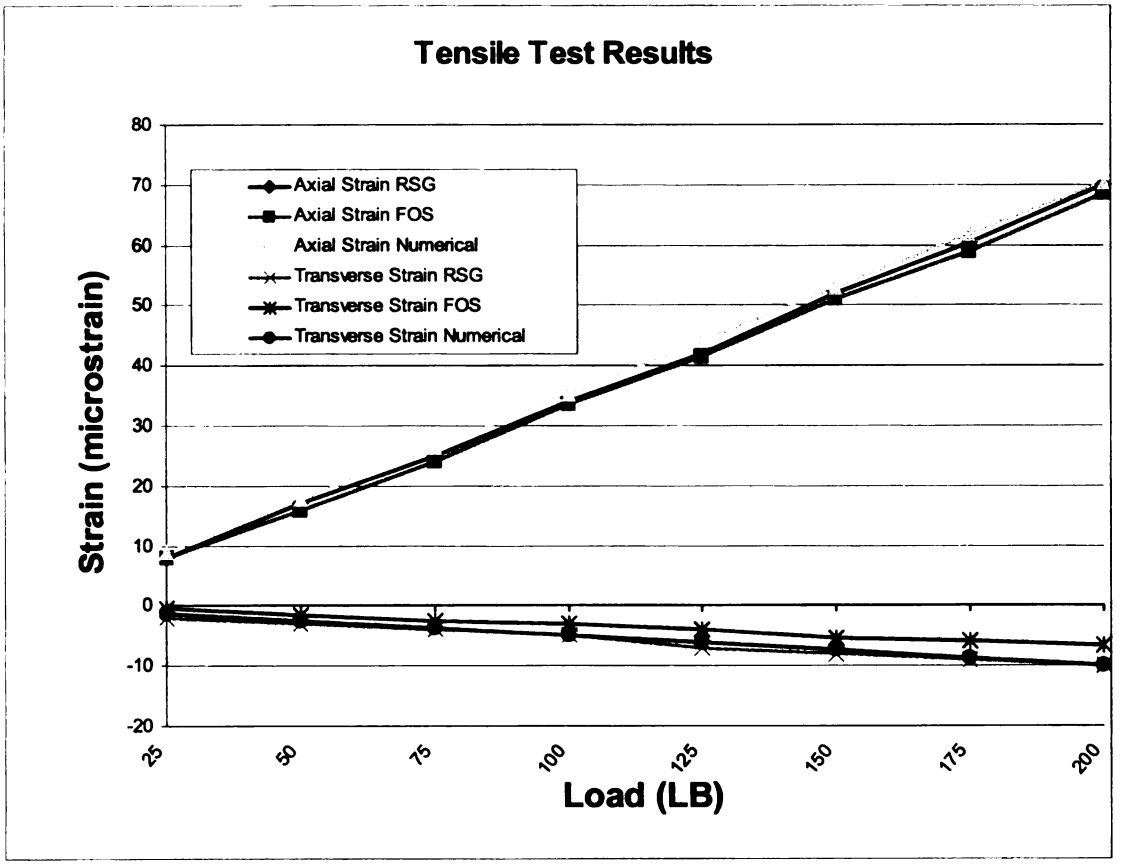

Figure 3.10 Tensile test result comparison.

Numerical results, resistance strain gage results and fiber-optic strain gage results show very good agreement for the longitudinal strains. Good agreement between numerical results and resistance strain gage results is shown for the transverse strains, with some discrepancies for the fiber-optic results. A possible reason for the difference in results is the very low value of strain for the transverse direction and the resolution difference for the two experimental techniques. The Measurements Group P-3500 Strain Indicator has a resolution of

1 με and the FISO UMI-8 has a resolution of 0.5 με. Error sources are addressed in more detail in Chapter 7.

Table 3.4 shows a comparison between the analytical and experimental determinations of the Poisson ratio ν_{12} and the elastic modulus along the direction of the fibers.

	Analytical	**RSG result**	**FoSG result**
E_1 (e6 PSI)	2.466	2.47	2.62
ν_{12}	0.14	0.15	0.11

Table 3.4 Material properties validation.

Overall the results show generally a good agreement that prove that the material properties used in the finite element numerical model are accurate. Also, the fiber-optic strain gages proved to be a solid and efficient tool in studying composite laminates strain fields.

3.3 CLAMPING FORCE DETERMINATION

A torque wrench was used to apply a preset torque on the bolt head. This torque has to be converted to clamping force. The clamping force is one of the most important parameters in this study and represents the force exerted by the bolt on the two plates that form the bolted joint, holding them together. This parameter has to be introduced into the finite element model and its value greatly influences the analysis.

In the "Standard handbook of fastening and joining" (1989) the following formula is given:

$$T=K\cdot D\cdot P \qquad 3.3$$

where T=installation torque (lb-in)

K=torque coefficient

D=nominal bolt diameter (in)

P=clamping load (lb)

In the formula above the only variable is the torque coefficient. This coefficient varies with a multitude of parameters including finishes, wear, lubricant coatings, etc. The variation of the torque coefficient can only be

determined experimentally. For some of the standard fasteners statistic analysis was used to determine the range in which the torque coefficient is most likely to fall.

For the purpose of this research, accurate determination of the clamping load was performed by using Transducer Techniques THC-1K-T 1000lb thru-the-hole type load cell transducer, as shown in Figure 3.11. The transducer is used in combination with a Hewlett-Packard 6200B DC power supply and a Hewlett-Packard 3468A multi-meter.

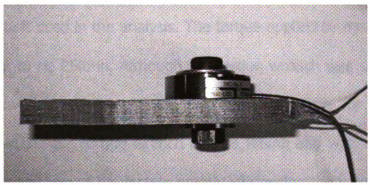

Figure 3.11 Load cell transducer.

The load cell calibration was checked using shunt resistors, and calibration data was compared against the manufacturer's supplied calibration sheet. The comparison between the two calibration curves is shown in Figure 3.12. The measured difference between the calibration values was less than +/-0.3%.

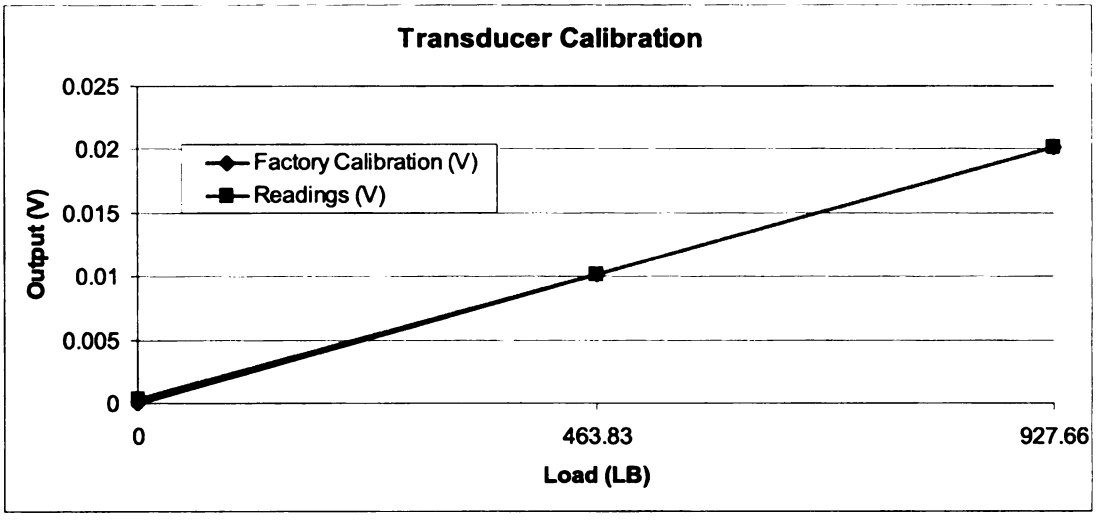

Figure 3.12 Transducer calibration.

A series of forty successive load-unload cycles were performed with a 0.5in shoulder bolt used in the analysis. The torque applied by means of a torque wrench was set to be 25lb-in. Although the torque wrench was set to a specific value, the converted clamping force was not the same for two or more consecutive tightenings. Torque wrench release timing and wear of the nut and bolt threads are just two of the factors greatly influencing the results.

A few tests were done concerning the clamping load. The transducer was mounted on a similar specimen using the same nut and bolt as used in the single-lap joint. The bolt was tightened using the torque wrench and the clamping load values were read after a five minute interval. After the reading the bolt was released and then a new tightening was performed with the same

parameters. Forty such cycles were done for each test. A sample result is shown in Figure 3.13.

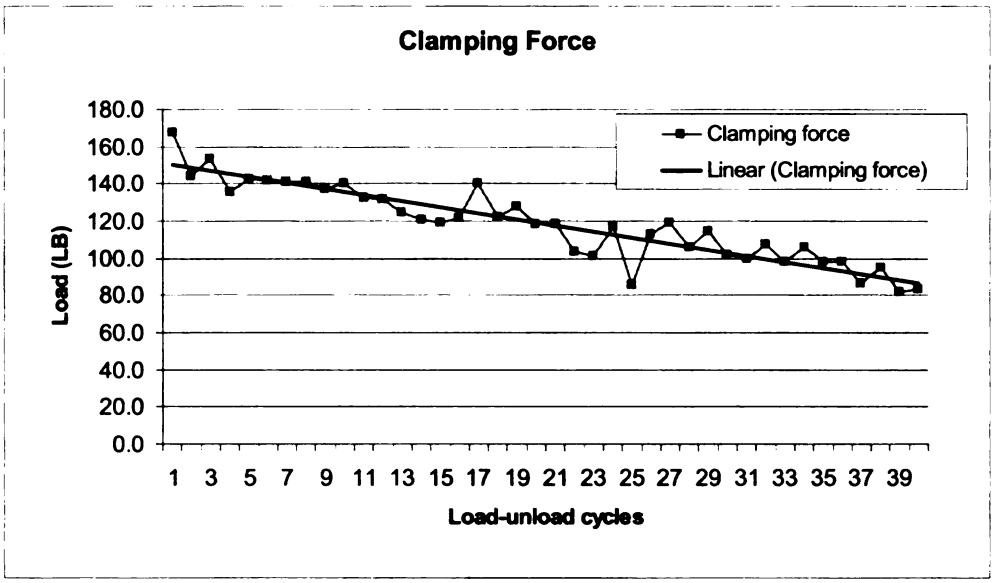

Figure 3.13 Clamping force variation for successive 25lb-in bolt torque applications.

This development led to modifications in the way the experiment was run. A longer bolt was used to allow mounting of the load cell transducer directly on the bolted joint. This change provided the means to read the clamping force in a direct manner during the load-up sequence. A special configuration was necessary to ensure that the bolted joint configuration would not be influenced by the addition of the transducer.

Experiments performed with the modified setup to accommodate the transducer showed a pattern in clamping force variation or relaxation. The relaxation was attributed, in principal, to the soft nature of the composite matrix. Readouts from two experiments are shown in

Figure 3.14. The experiments were conducted in such manner as to allow sufficient time for material relaxation between two consecutive experiments. Two very important conclusions were drawn:

- Initial clamping load varies at the same torque setting;
- Clamping force relaxes over the duration of the experiment.

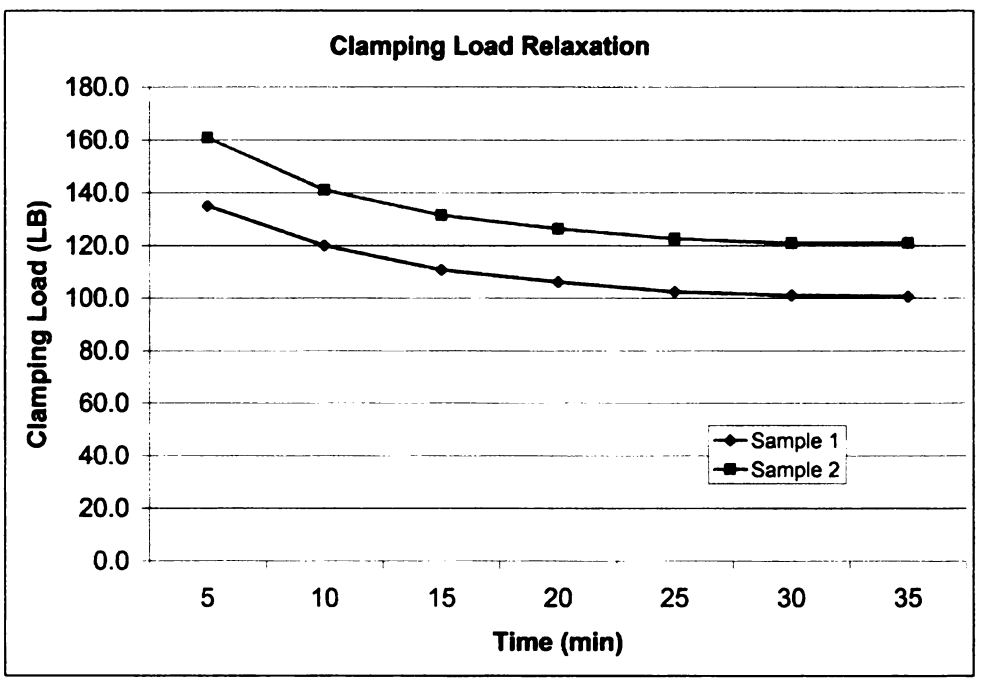

Figure 3.14 Clamping force relaxation.

3.4 EXPERIMENTAL ANALYSIS

As stated in the Research Objectives, one of the goals of this research study was to obtain through-the-thickness strain measurements that would validate the finite element analysis. In turn, the finite element model, validated by experimental data, delivers the locations of the maximum shear stress and of the possible failure of the composite plate.

The supporting plate was made of aluminum 2024-T4 with the following material properties:

$$E = 1.01e7 \text{ psi}$$

$$\nu = 0.34$$

The aluminum plate used in the investigations was 8inx4inx0.5in (Length x Width x Height).

Fiber-optic strain gages were embedded in the composite specimens at the time of fabrication. The detailed process and guidelines for fabricating such specimens can be found in Appendix 1.

Experiments performed in this study used specimens that incorporated different numbers of fiber-optic strain gages. One of the first specimens

contained only one fiber-optic strain gage and it was built to assess whether or not fiber-optic strain gages can deliver results from an area that has very high strain gradient. Another reason was to make an initial qualitative assessment of the experimental data coming from a composite plate used in a bolted joint. The initial assessment validated the use of fiber-optic strain gages placed close to the bolt hole. Since the results obtained from the specimen having only one fiber-optic strain gage were only qualitative, they were not presented in this thesis.

The next step was molding specimens that had more measurement points so that the strains in the bearing plane of the composite plates can be compared with the finite element models. The decision made was to use three fiber-optic strain gages embedded in the bearing plane of each composite plates at safe distances from the bolt hole and the surfaces. All specimens in this first batch had three embedded fiber-optic strain gages and will be named *Type 1* Specimens from now on. One of the fiber-optic strain gages attached to the E-glass weave is shown in Figure 3.15a. The approximate position of the sensors is shown in Figure 3.15b and the specific location and strain gage identification are shown in Figure 3.15c.

Problems experienced during experiments performed with the *Type 1* specimens included strain gage damage during hole drilling or manufacturing, precise strain gage positioning and optical fiber shear at the exit point from the

specimen. All these issues were fixed for the specimen used in the final stage of the research.

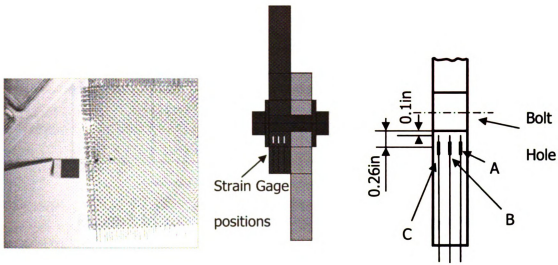

(a) (b) (c)

Figure 3.15 *Type 1* Specimens: (a) Fiber-optic strain gage attached to the E-glass weave; (b) schematics of the sensor locations; (c) sensor locations and identification.

The dimensions of the *Type 1* specimens are shown in Figure 3.16. As is can be observed, the specimens were 5in long. This created problems because of the insufficient space to route the optical fiber coming out of the specimens. A lower corner radius had to be used for the fiber, creating unnecessary stress on the fiber at the specimen interface. The additional stress lead to fiber rupture in a few cases.

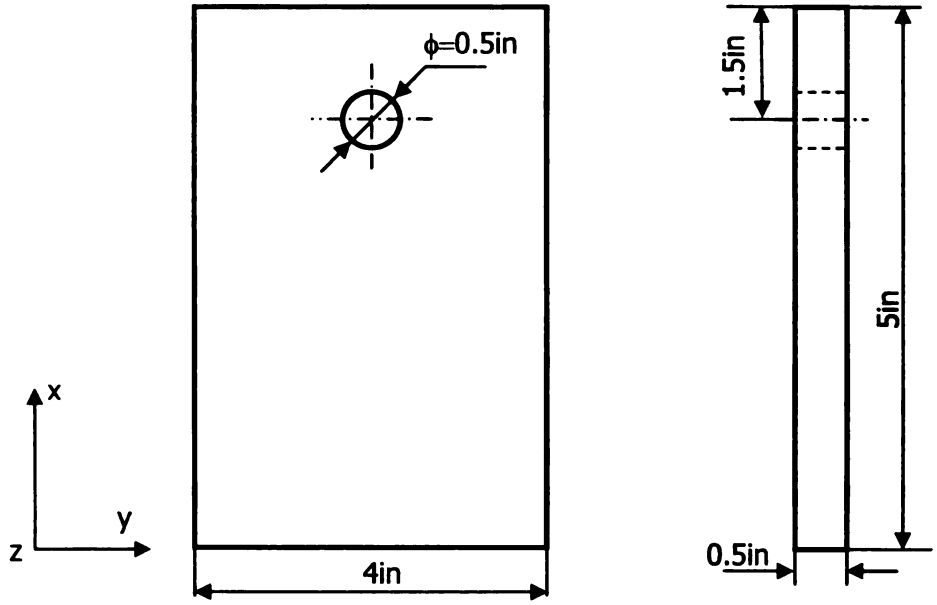

Figure 3.16 Specimen dimensions for the *Type 1* specimens.

The composite specimen used in the final stage of this research study was 8inx4inx0.5in (Length x Width x Height). This specimen will be referred to as *Type 2* specimen. Material properties for the composite plate were identical as the first batch specimens and were presented in subchapter 3.2. Detailed dimensions of both aluminum and composite plates are show in Figure 3.17.

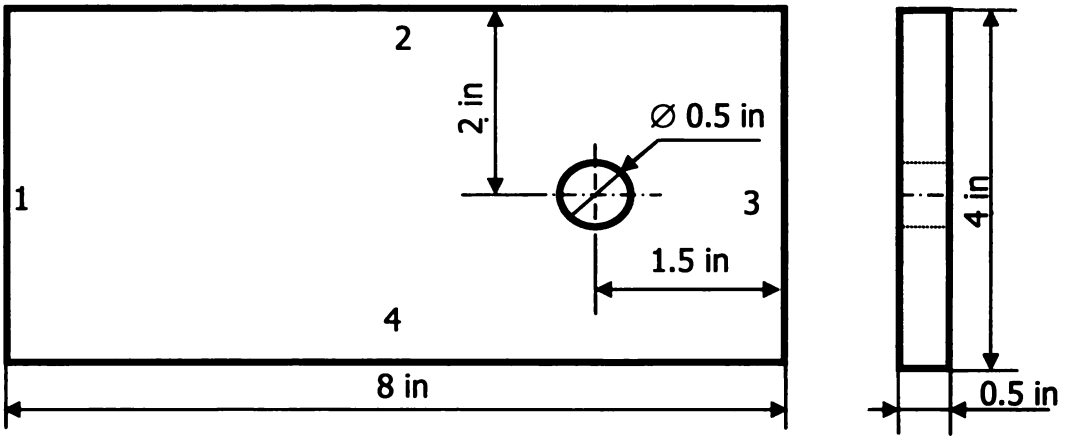

Figure 3.17 Dimensions for the aluminum plate and *Type 2* specimen.

The experience gained with the *Type 1* specimens proved to be very useful when new specimens were fabricated. Precise location of the fiber-optic strain gages is very important and special techniques were used to improve sensor positioning such that hole drilling did not affect the sensors. Details about sensor positioning are found in Appendix 1. Protection measures were added to ensure the integrity of the optical fiber at the specimen interface. Shrink wrap tubing was added to the vulnerable part of the optical fiber for protection. One such installation was shown in Figure 3.6.

The locations of the five sensors embedded in the specimen are shown in Figure 3.18.

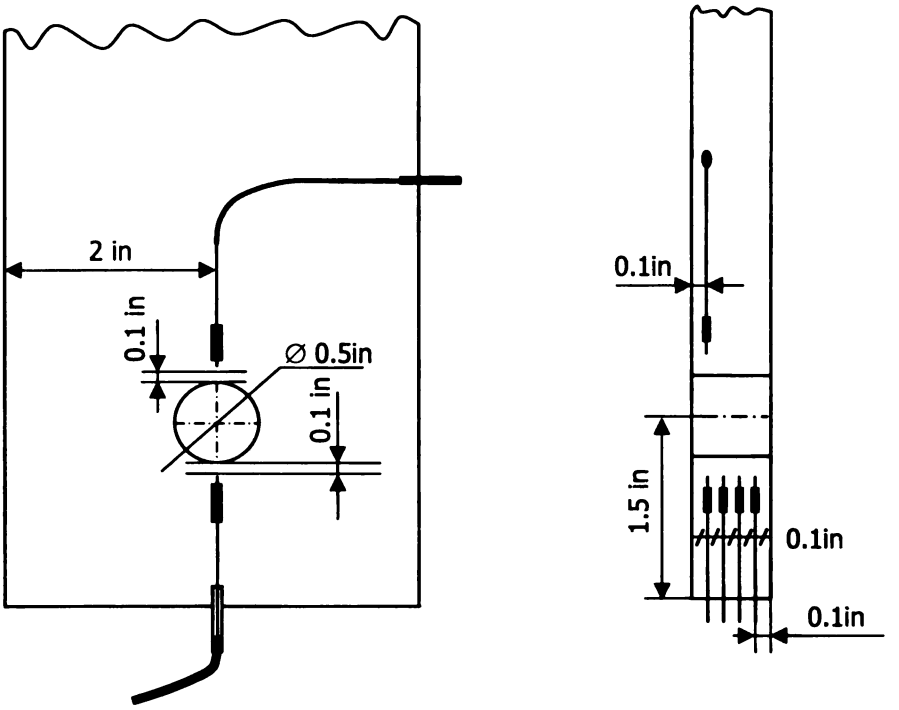

Figure 3.18 Fiber-optic strain gage locations in the *Type 2* specimen.

The bolted joint was subjected to axial load on a loading frame as shown in Figure 3.19 and Figure 3.20. The axial loading was performed by adding dead weights on the loading hanger. The loading frame has a mechanical advantage factor of 5. For each pound of deadweight on the loading hanger, a load of 5lb is exerted on the bolted joint. The bolted joint equipped with the transducer and in loading position is shown in Figure 3.20.

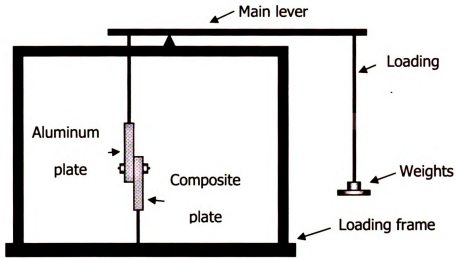

Figure 3.19 Loading frame schematics.

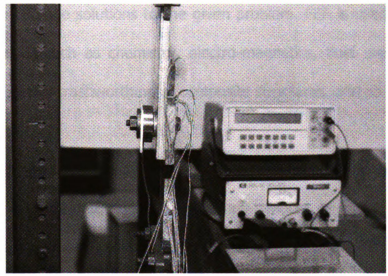

Figure 3.20 Bolted joint with transducer – loading frame position.

A comparison and discussion of the results obtained from experiments performed with both *Type 1* and *Type 2* specimens are presented in Chapter 5.

Chapter 4

FINITE ELEMENT MODELS

Finite Element Analysis (FEA) is one powerful tool that researchers are using with success to solve complex problems. Mathematical models are used to represent real-life phenomena and results obtained by solving the models represent approximate solutions to the given problem. FEA is used in numerous fields of research such as chemistry, electro-magnetics, fluid mechanics, solid mechanics, forming, crashworthiness, composite structures, and so on.

With the advance in computing performance, FEA becomes more and more important to the extent that it sometimes replaces expensive experiments. FEA is not recommended to be used as a whole means of obtaining results as it is, as previously stated, an approximation of the real life phenomena.

This research project combines experiments and Finite Element Analysis. The interaction between the two fields is mandatory for better understanding of localized phenomena and for validating results. As shown in Figure 4.1, Finite Element Analysis was used in close connection with the experiments. Feedback

from both methods provided enhancements and revealed possible causes of errors. The Finite Element Model was improved numerous times to better approximate the experiment conditions. In return, the Finite Element Analysis dictated improvements to the experiments including fiber-optic strain gage positioning.

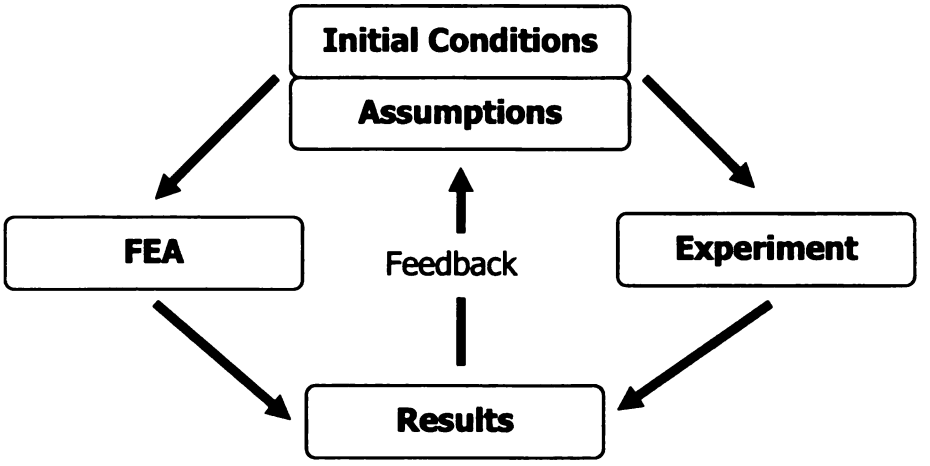

Figure 4.1 Validation scheme.

4.1 FINITE ELEMENT MODEL DESCRIPTION

Finite Element Analysis is a three step process. First a finite element model has to be built and load conditions applied. Second, the model is solved using one of the available algorithms. And finally, the third step is the processing and interpretation of the results.

During this research the software used for FEA simulations were ANSYS v9.0 – implicit finite element commercial code, and LS-DYNA v970 Rev5434 – explicit/implicit finite element commercial code. ANSYS is an all-in-one finite element software. It has built-in modeling capabilities, a powerful set of solvers that can handle diverse problems, and it also includes a built-in post-processor for result evaluation and interpretation. ANSYS can solve a wide range of problems including thermal, electro-magnetic, static (linear and non-linear), vibration, optimization and, with the LS-DYNA add-on module, dynamic problems. LS-DYNA is a very capable finite element code that can solve multi-physics problems including solid mechanics, crashworthiness, fluid dynamics, metal forming, heat transfer and others.

Both ANSYS and LS-DYNA were used in this research study. Initially, the FEA was performed exclusively in ANSYS. As the study matured, the need to implement special bolted joint characteristics, such as bolt-to-hole clearance, led

to the FE model migration from ANSYS to LS-DYNA. The reasons behind the migration are discussed further in this chapter. Both finite element models are discussed in detail.

4.1.1 ANSYS Finite Element Models

Initially, for this project, non-linear static analysis was required. Only implicit code was used due to the static nature of the problem. For dynamic calculations that take into account clearance and other complex factors, the model had to be migrated to use explicit code that can handle rigid body motion and large displacements.

One of the first models created was the tensile specimen used in validating the material properties and testing the fiber-optic strain gages. Material properties, once validated, were used in the bolted joint finite element model.

All models used SOLID45 three-dimensional structural solid elements. The tensile specimen was modeled using 750 SOLID45 elements of different dimensions. Coarse mesh was used at the ends of the coupon and finer mesh

was used in the center, where the area of interest was. Five elements were used for the thickness.

The boundary conditions were equivalent to the ones used in the experiment. The nodes on one end face were fixed and on the opposite end face nodal loads were applied. The model and the applied boundary conditions are shown in Figure 4.2.

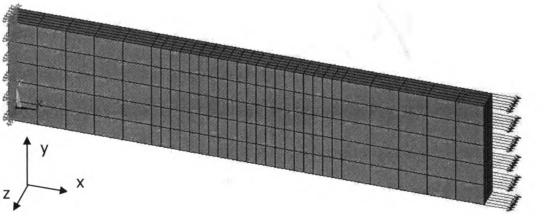

Figure 4.2 Tensile specimen model with applied boundary conditions.

Sample results obtained using the finite element model for the tensile specimen can be seen in Figure 4.3.

A comparison between finite Element Analysis, fiber-optic strain gages and resistance strain gages was presented in Chapter 3.

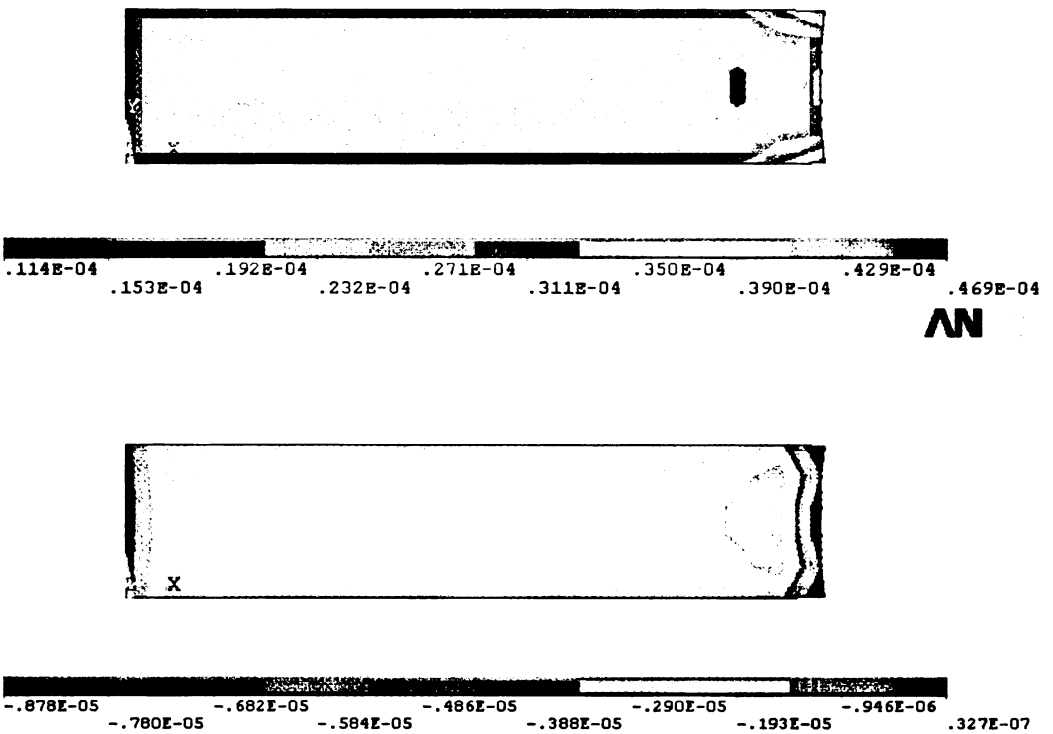

Figure 4.3 Longitudinal (top) and transverse (bottom) strains for 50lb load (in strains).

With preliminary determinations finished the finite element model of the bolted joint was prepared.

The bolted joint was modeled using SOLID45 8-node elements. Special attention was dedicated to the meshing process. This step is very important because of significant impact it has over calculations.

Since the bolted joint has a plane of symmetry, the model created was half of the bolted joint. Symmetry boundary conditions were used on the symmetry plane. A typical mesh is shown in Figure 4.4.

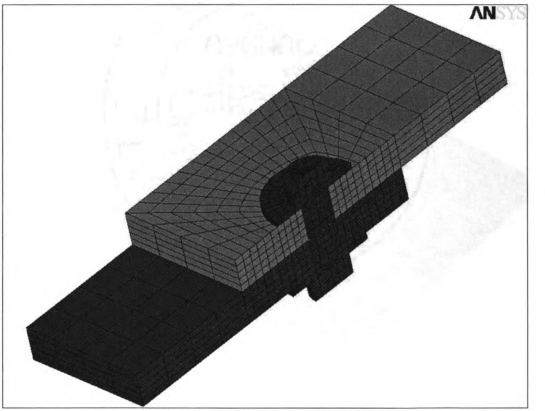

Figure 4.4 Meshed bolted joint.

One of the most important advantages of working with only half the model is the reduction in the number of elements. This leads to a direct reduction of the number of equations which translates into greatly reduced computational time. The model can be expanded symmetrically to represent a full-shape model. A symmetry expansion of the half-model is presented in Figure 4.5.

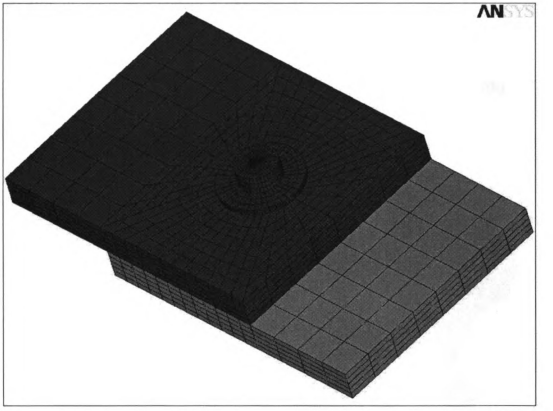

Figure 4.5 Symmetry expansion mesh.

Each plate was split into separate volumes for easier and more accurate meshing. The split-volume technique helped in reducing and eliminating shape-violating elements. Another fact worth mentioning is meshing the high strain gradient regions with smaller elements and lower gradient regions with larger size elements. This led to a better distribution of the number of elements and not only reduced the size of the model but provided good indication of contact issues arising from mesh generation gaps and penetrations. A close-up view of the mesh around the hole is shown in Figure 4.6.

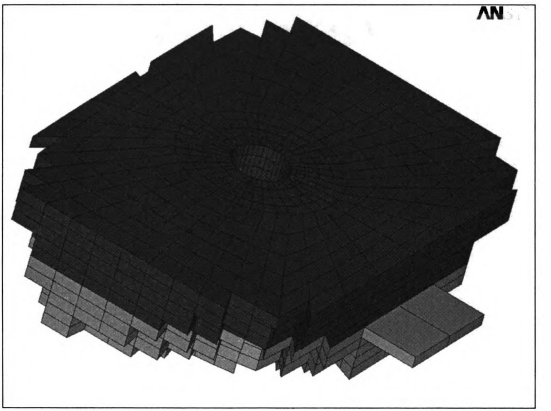

Figure 4.6 Close-up view of selected elements around the bolt hole.

To reduce the number of contact surfaces included in the model, and for simplification reasons, the bolt, nuts and washers were all modeled as a single volume. The bolt, nut and washer assembly is shown in Figure 4.7. The bolt hole diameter has the same value as the bolt shank to simulate a snug fit. This was also important because of contact convergence constraints.

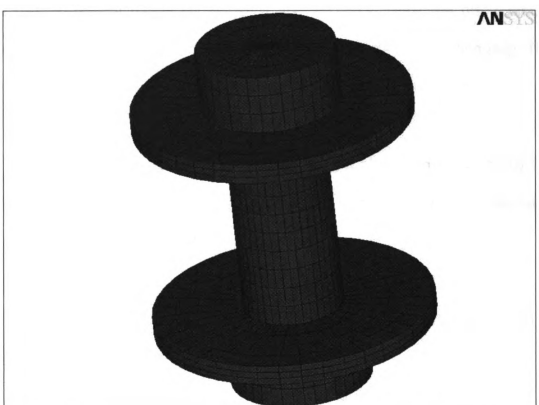

Figure 4.7 Bolt, washer and nut assembly.

Since the finite element model is used to simulate both pin connection and bolt connection, pretension had to be introduced. There are multiple ways to simulate bolt pretension using finite element models. Most common methods

are: thermally induced pretension, washer/nut pressure and pretension by special elements. The latter uses specially designed elements that achieve the desired pretension by creating a virtual section within the bolt shank. The virtual section splits the bolt in two and then it brings them together using the desired clamping force value. The pretension effects needed to be calculated in the first loading step of the simulation. No other external loads were introduced during this step to ensure model convergence and accuracy. Once the displacement map was calculated it was used as initial condition for the next loading step. The subsequent loading steps were used to apply load on the bolted joint.

The pretension section is meshed using special elements. In ANSYS the pretension elements are PRETS179. The location of the section cut (pretension mesh) was specified as a fixed value on the bolt shank.

A simplified scheme on how the pretension was achieved using PRETS179 elements is shown in Figure 4.8.

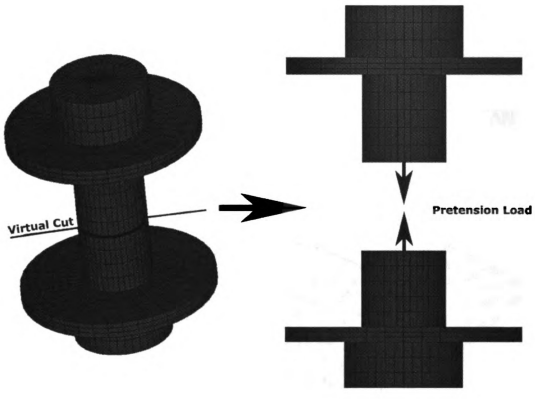

Figure 4.8 Bolt pretension scheme.

ANSYS introduces a new way of modeling contact by laying the contact elements on top of the solid mesh. The contact elements used were selected based on the three-dimensional characteristics of the model and also based on the nature of surfaces coming in contact. Elements having surface-to-surface capabilities were used to model the contact surfaces. In ANSYS, contact surfaces are designated as *Target* and *Contact* surfaces. This is analogous to the master/slave scheme. Target surfaces are the equivalent of slave surfaces and contact surfaces are equivalent to master surfaces. Each target and contact surface coming in contact forms a *contact pair*. All contact pairs were modeled as

flexible-to-flexible contact pairs. Contact surfaces for the expanded model are shown in Figure 4.9.

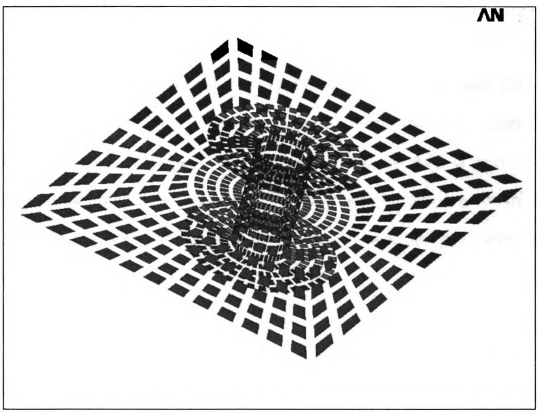

Figure 4.9 Contact surfaces (element shrinkage used for better visualization).

- Contact pairs were formed as follows:
- Washer to plate (2 pairs)
- Bolt to hole (2 pairs)
- Plate to plate (2 pairs)

Some clarifications are necessary for the number of contact pairs. Contact between each washer and the small cylindrical volume under the washer is modeled as one contact pair. The bolt surface and the hole of each plate constitute one contact pair. Because of the split volume nature of the model, there are two pairs of surfaces coming into contact between the two plates, thus forming two contact pairs.

Elements used to model the contact surfaces are CONTA174. These elements are three-dimensional, have 8 nodes, and are used for surface-to-surface contacts. The target surfaces were meshed using TARGE170. These elements are three-dimensional and take the number of nodes of the element upon which they are laid .

The contact method of choice was the Augmented Lagrange Method. This method is basically the same as the Penalty method with enhanced penetration control. The reason behind the choice was the better conditioning and decreased computation time of the method, capability to handle large displacements and

the handling of contact surfaces coming in and out of contact. The behavior of the contact pair was set to standard. The option to automatically close gaps and reduce penetration was enabled. The option to exclude initial penetration was enabled.

Fiction coefficients were assigned separately for each contact pair. The friction coefficient for steel-aluminum contact was set to 0.3. The friction coefficient for both aluminum and steel with the composite plate was set to 0.48. The influence of friction coefficients on the FEA results is discussed in Chapter 7. Contact surface status was checked before each simulation to reveal gaps or penetrations. ANSYS can automatically offset surfaces so they come in contact if the gap in a contact pair is reasonably low.

The boundary conditions applied to the finite element model simulated in detail the experimental conditions. The composite plate was fixed to the free end. Symmetry conditions were applied for all parts on the symmetry plane. Clamping force was simulated as pretension in a separate loading step. The aluminum plate had all nodes from the free surface coupled to simplify load application and to avoid unwanted edge deformation. A master node was assigned and a single force was applied to it. Multiple load steps were necessary to obtain the necessary results to match the experimental loading conditions.

The final finite element model incorporated 4723 elements and it is shown with applied boundary conditions in Figure 4.10.

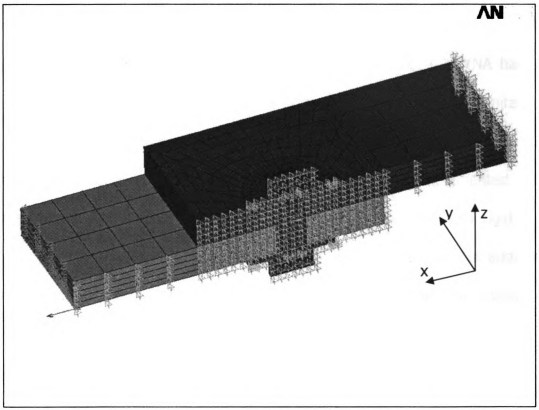

Figure 4.10 Finite element model of the bolted joint with boundary conditions and load.

Results and discussion on the results obtained with the ANSYS finite element model are presented in the next chapter.

4.1.2 LS-DYNA Finite Element Models

LS-DYNA was used as a useful tool to bridge the gap between the limitations of the ANSYS models and the real-life situations. LS-DYNA handled problems where ANSYS could not converge due to implicit code limitations. Change in surface contact status (on/off) and bolt-to-hole clearance were just two very important real-life situations that could not be implemented using ANSYS alone. The ANSYS models were migrated to LS-DYNA and rigid body motion, change in contact status and clearance were handled without additional spring elements, very soft materials or other improvisations. The mesh was exported from ANSYS using the ANSYS/LS-DYNA module. With the mesh in place, the models were then imported in Altair HyperMesh v7.0 modeler where contact, boundary conditions, loads and all other necessary LS-DYNA "keywords" (commands) were introduced.

Two cases were modeled in LS-DYNA. The first model simulated a pin connection. This case was simulated because the only load present was the load applied to the joint. This step was necessary to avoid any possible problems caused by the clamping force.

LS-DYNA Pin Connection Model

The pin connection model consisted of three parts: the aluminum plate, the composite plate and the pin. All parts were modeled using SOLID elements. SOLID elements were required because of the three-dimensional nature of the problem. SHELL elements would not have sufficed because they cannot accurately simulate the contact between the plates and the pin. The LS-DYNA pin connection model is shown in Figure 4.11.

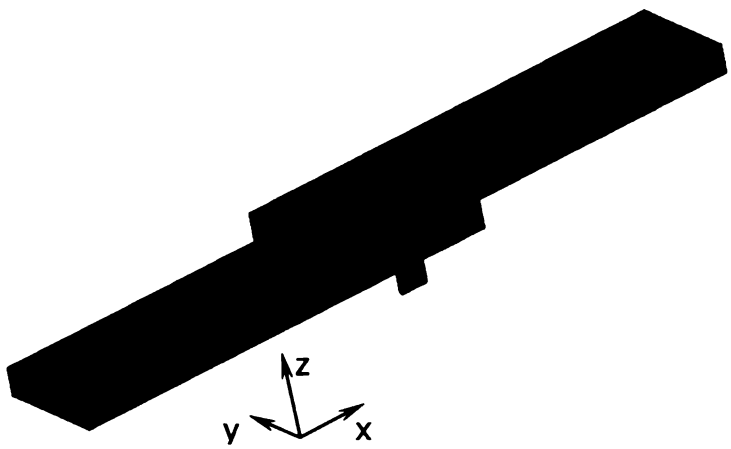

Figure 4.11 LS-DYNA pin connection model.

The pin connection model had 5138 nodes in 4020 elements. All elements were considered deformable, including the pin. Material properties for the aluminum plate and the pin were defined using *MAT_ELASTIC card. Because

during the experiments the loads used were not causing any plastic deformation to the joint components, plasticity was not considered. The composite plate was modeled using *MAT_ORTHOTROPIC_ELASTIC card.

The mesh was refined for both plates in the area around the bolt hole. The pin mesh was adapted to the hole mesh such that there were equal numbers of elements for the hole and the circumference of the bolt. This was important to minimize node-to-element penetrations during the contact.

Contact between the two plates and between the two plates and the bolt was simulated. The contact option used for the model was chosen based on the nature of the contact. *CONTACT_SURFACE_TO_SURFACE_ID was preferred. This way, contact surfaces were defined using SET_SEGMENT and then pairs were formed to create the full contact definition. Three contact pairs were created as follows:

- aluminum plate to composite plate,
- pin to composite plate,
- pin to aluminum plate.

All contact pairs were governed by the master-slave principle. The surfaces belonging to the stiffer material were considered master contact

surfaces. The friction coefficient for steel-aluminum contact was set to 0.3. The friction coefficient for both aluminum and steel with the composite plate was set to 0.48. This was consistent with the ANSYS model.

Since there were no rigid elements present, all parts were considered deformable and a more accurate representation of the physical interactions present in the bolted joint was obtained.

A close-up view of the region around the pin is shown in Figure 4.12.

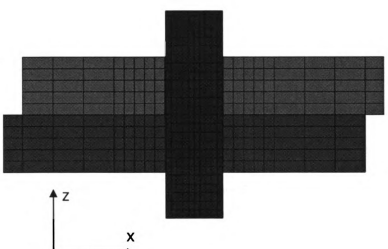

Figure 4.12 LS-DYNA pin connection model: close-up view.

Bolt-to-hole clearance was set for both the aluminum and the composite plates. Diametric bolt-to-hole clearance values were set to 0.01in for the aluminum plate and 0.005in for the composite plate. The clearance values were

selected for reasons explained in Chapter 5. No clearance was modeled for the contact between the two plates. The initial penetration check option was activated in the contact definitions to verify that no nodes or elements were penetrating the opposing contact surface.

Boundary conditions were defined using three node sets. The node sets were useful because they simplified the load definitions in the LS-DYNA input file.

The far end of the composite plate was set to have zero translation for all three axes. Rotation was permitted around any axis, similar to the experiment conditions.

A half model approach was used to take advantage of the symmetry plane present in the pin connection model. Symmetry boundary conditions were applied to all nodes in the symmetry plane. The load was applied to the far end of the aluminum plate by means of a load curve with predefined points for specific load values, similar to the experiment loading conditions. No additional loads were applied. Except for the mentioned nodal constraints and symmetry conditions, no other nodal constraints were present.

LS-DYNA Bolted Joint Model

The second LS-DYNA model was used to simulate the bolted joint case. The model was created in a similar manner as the pin connection model. The differences and similarities between the two models are explained below.

The bolted joint was modeled using 4496 nodes in 3290 elements. All elements were SOLID type similar to the pin connection model. Material properties were the same as for the pin connection case.

The bolt, washers and nut representing the bolt assembly were modeled as a single part, to minimize the number of contact surfaces and processing time.

In addition to the three contact pairs present in the pin connection model, two more contact pairs were needed to account for the two washer-plate interactions. These surfaces were modeled similar to the existing three pairs, using the *CONTACT_SURFACE_TO_SURFACE_ID contact card. The LS-DYNA bolted joint model is shown in Figure 4.13.

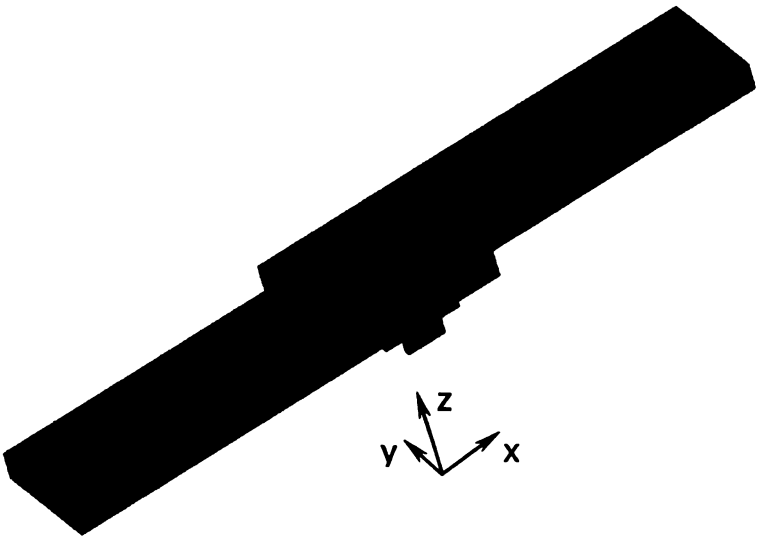

Figure 4.13 LS-DYNA bolted joint model.

The bolt pretension was obtained using a newly introduced option in LS-DYNA 970 Rev 5434. This option defines an initial stress section in a selected part set. The initial stress section acts in a similar manner as the ANSYS pretension mesh. A part set is defined and it can contain one or more parts. The part set is virtually separated with a plane defined in *DATABASE_CROSS_SECTION_PLANE card. The two portions of the part set will then be forced to come together and in this way the pretension is obtained. A stress curve with zero origin and the desired maximum value needs to be applied to the part set. When the end of the stress curve is reached, the pretension initialization stops and the joint load can be applied.

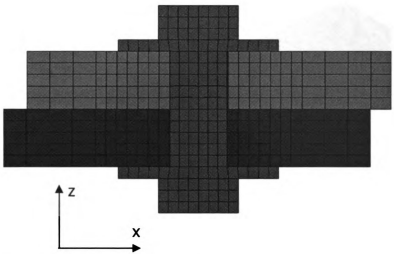

Figure 4.14 LS-DYNA bolted joint model: close-up view.

The initial stress section option is similar to the ANSYS pretension mesh but it differs in the way the pretension value is defined. The ANSYS pretension is achieved by specifying a load value whereas the LS-DYNA pretension is achieved by specifying a desired stress value. Since the experimental values for pretension are in terms of clamping force, a transformation from force to stress is necessary to achieve a similar result.

A full model of the bolted joint created by symmetry expansion is shown in Figure 4.15.

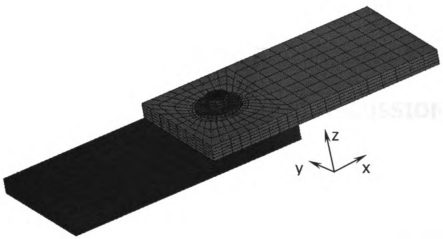

Figure 4.15 LS-DYNA bolted joint model: symmetry expansion.

The boundary conditions for the bolted joint were set similarly to the ones defined for the pin connection model. The far end of the composite plate was constrained for translation along all axes and free to rotate. Symmetry boundary conditions were applied to the nodes in the symmetry plane and the axial load is applied using a load curve. The load curve was set so that it was zero until the pretension stage ended.

Chapter 5

RESULTS COMPARISON AND DISCUSSION

Results from experiments and Finite Element Analysis are compared in this chapter. Results for the pin connection and the bolted joint are presented. Results are presented separately for *Type 1* and *Type 2* specimens.

5.1 RESULTS FOR TYPE 1 SPECIMENS

Type 1 specimens provided useful data in the first stages of this research. Experiments conducted with these specimens recorded data for positions A, B and C, as shown in Figure 3.15. No pin connection data was compiled for *Type 1* specimens. The optical fibers of the embedded sensors in *Type 1* specimens were damaged during various stages of the experiments and data was available only for the 25lb-in bolt torque. Fiber-optic sensors were not reset after the torque was applied. A comparison between finite element results and experimental results for the 25lb-in bolt torque is shown in Figure 5.1.

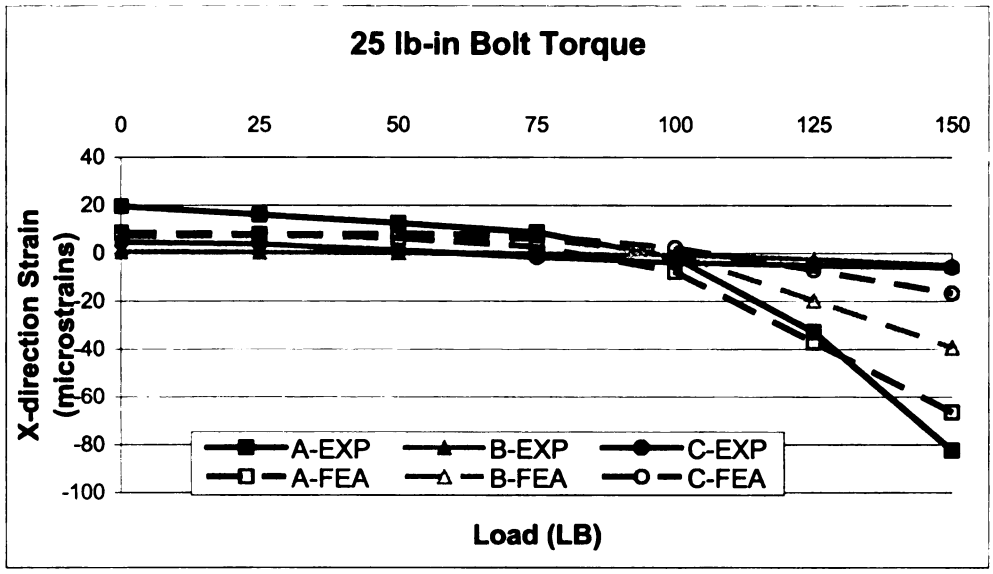

Figure 5.1 Results comparison for *Type 1* specimens: ε_{xx} (25lb-in bolt torque) – one sample experiment.

The results for the *Type 1* specimens show a fairly good correlation for strain gages in positions A and C. The strain gage in position B showed a fairly large discrepancy compared with the finite element results. Also, experimental data showed a slightly different trend than was obtained with finite elements. Multiple experiments were performed and initial strain scatter appeared after the bolt torque was applied. The differing trends and the initial strain scatter were caused by visco-elastic effects in the composite plate matrix. These effects were mentioned in subchapter 3.3 Clamping Force Determination.

A strain map of the axial strain (ε_{xx}) obtained from FEA is shown in Figure 5.2. The maximum compression strain occurs at the initial contact point which is on the edge of the hole. The ANSYS model does not have any bolt-to-hole clearance, but clearance is actually present in the experiment.

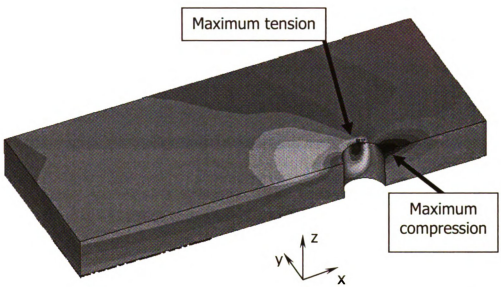

Figure 5.2 *Type 1* specimens: ε_{xx} strain map for 150lb load and 25 lb-in bolt torque.

A full size strain map of the axial strain (ε_{xx}) at 150lb load is shown in Figure 5.3. The full size map was created by symmetry model expansion within the ANSYS post processor. The advantage of the full symmetry expansion is that it creates a full picture of the strains sustained by the object. A half size model is also useful because, in our case, it shows the strain distribution in the bearing plane.

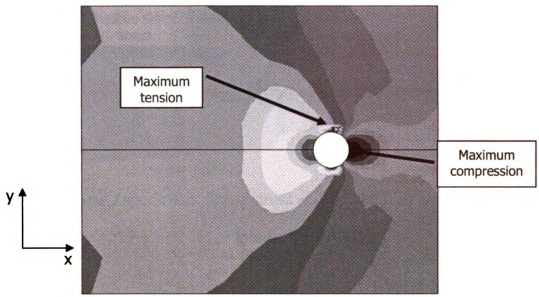

Figure 5.3 *Type 1* specimens: symmetry expansion of the ε_{xx} strain map for 150lb load and 25lb-in bolt torque.

A shear stress map of the σ_{xy} shear stress at 150lb load is shown in Figure 5.4. The maximum shear stress σ_{xy} in the composite plate provides indication on where initial delamination will first occur if the specimen is overloaded. The failure is likely to develop at an angle of approximately 45° from the x-direction. This is a very important factor in safety calculations for such joints.

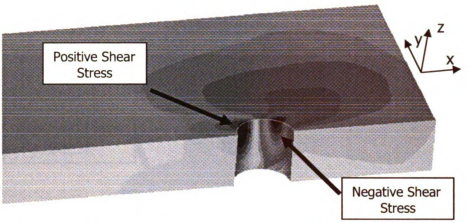

Figure 5.4 *Type 1* specimens: Shear stress σ_{xy} at 150lb load and 25lb-in bolt torque.

The von Mises stress distribution in the bolt assembly reveals a maximum stress occurring on the composite plate side of the built-in washer, as shown in Figure 5.5. This is expected as the bolt tilts under the load. The maximum von Mises stress on the composite plate occurs on the side of the bolt hole in the area with maximum tensile strain.

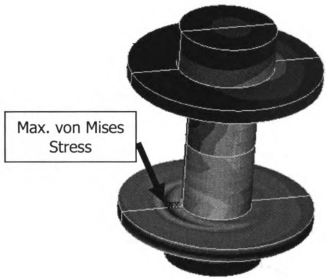

Figure 5.5 *Type 1* specimens: von Mises stress map in the fastener at 150lb load and 25lb-in bolt torque.

A complete strain map of the bolted joint for *Type 1* specimens showing the axial strain at 150lb load and 25lb-in bolt torque is shown in Figure 5.6.

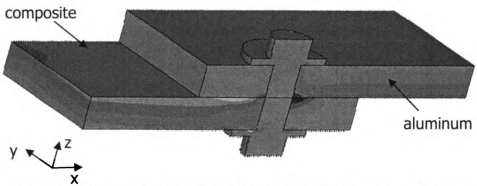

Figure 5.6 ε_{xx} strain map of the bolted joint for 150lb load and 25lb-in bolt torque.

5.2 RESULTS FOR THE TYPE 2 SPECIMEN

Experiments with the *Type 2* specimen, although the same in nature as the experiments with *Type 1* specimens, followed different procedures. These procedures were implemented out of the need to overcome problems related to clamping force relaxation, creep, and strain scattering. These procedures were improved as more experiments were performed. The procedures included the use of a conical spring washer to compensate for the clamping force relaxation, accelerated load/unload process and strain gage resetting. All finite element results for the *Type 2* specimens were extracted using LS-DYNA.

In order to eliminate undesired effects of the strain components created by the clamping force, the results for the pin connection experiments and LS-DYNA pin connection model were compared. The schematics and the labels of the equivalent positions of the fiber-optic strain gages in the finite element model are shown in Figure 5.7. The locations and labels are valid for the pin connection case as well as the 25lb-in bolt torque case.

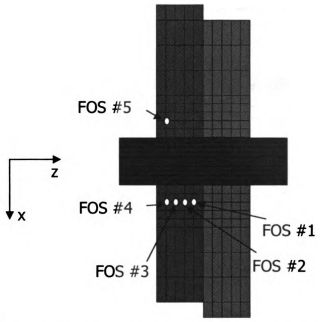

Figure 5.7 Equivalent positions of the fiber-optic sensors for *Type 2* specimen.

A comparison between the finite element results and the experimental data is shown in Figure 5.8. The experimental data were recorded for multiple experiments and then averaged. The graph shows the averaged experimental data.

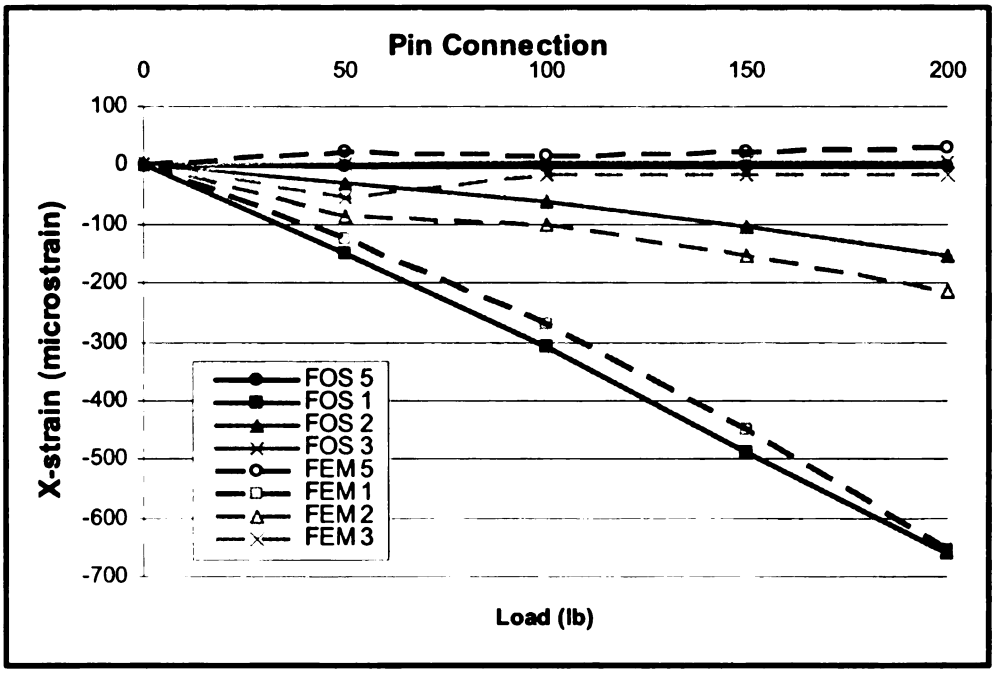

Figure 5.8 Results comparison for *Type 2* specimen: ε_{xx} for the pin connection case.

Fiber-optic strain gage number 4 was damaged during the fabrication process, therefore results for that particular location were not available. Since no correlation can be made between the finite element results at the FOS#4 location and the experimental data for FOS#4, finite element results for FOS#4 were not compiled.

The experimental data and the finite element results for the pin connection agreed reasonably well. The maximum strains present at the edge of the composite specimen bolt hole were successfully characterized. A slightly larger difference was observed for the other locations.

The maximum axial strain, in the bearing plane of the composite plate, was recorded by FOS#1 and the value was -662 με. The finite element model results showed -653 με for the same position. The difference between the experiment and the finite element analysis is lower than 1.5%.

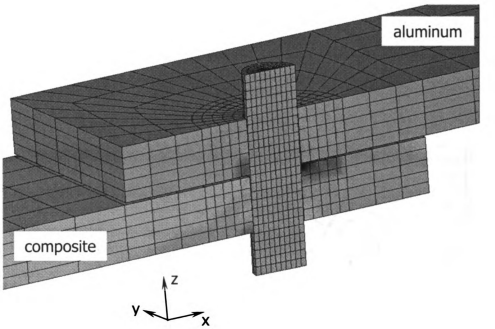

Figure 5.9 Pin connection: ε_{xx} strain map for *Type 2* specimen at 200lb load.

Axial strains of the pin connection for 200lb load are shown in Figure 5.9. The plates were modeled as being in contact at the start of the finite element simulation. As the load increased, the plates were forced out of contact until total separation was achieved. This observation was consistent with experiments.

Another important factor that needed attention was the value of the bolt-to-hole clearance. Initially, clearance values were set to be the same for both the aluminum and the composite plates. This contradicted the experiments which were showing compression strains present at the location of FOS#5. The LS-DYNA model was modified accordingly to allow the pin to have a secondary contact point on the composite plate.

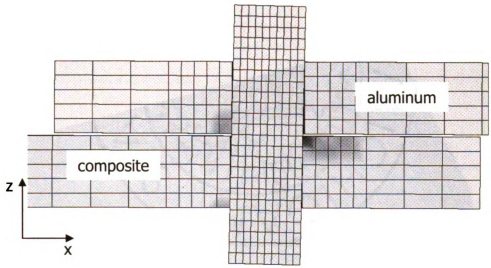

Figure 5.10 Pin connection: ε_{xx} strain map with visible secondary contact point at 200lb load.

A close-up view of the pin connection showing axial strains at 200lb load is shown in Figure 5.10. The picture shows the two regions of contact for the

composite plate and the total separation of the plates under load. The aluminum plate was found to be controlling the motion of the pin and the contact between the pin and the composite plate.

A stand-alone view of the composite plate strain field of axial strains at 200lb load is shown in Figure 5.11. The maximum strains occur at the edge of the plate where the pin contact patch begins. Tension strains present on the sides of the hole are caused by the axial load being mainly supported by only one side of the hole.

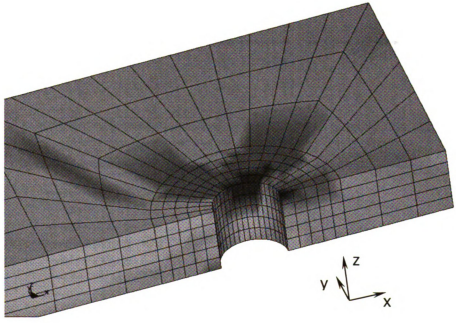

Figure 5.11 Pin connection: *Type 2* specimen ε_{xx} strain map at 200lb load.

Changes in bolt-to-hole clearance in the pin connection finite element model were propagated to the bolted joint model.

Fiber-optic strain gages were reset to zero after the bolt torque application. Undesired strains caused by visco-elastic effects were minimized this way.

A comparison between the finite element results and the experiments is shown in Figure 5.12. The bolted joint was loaded from 0lb to 200lb and data from multiple experiments were averaged. The experimental results shown in the graph are averaged results. Good validation for the maximum strain in the bearing plane can be observed.

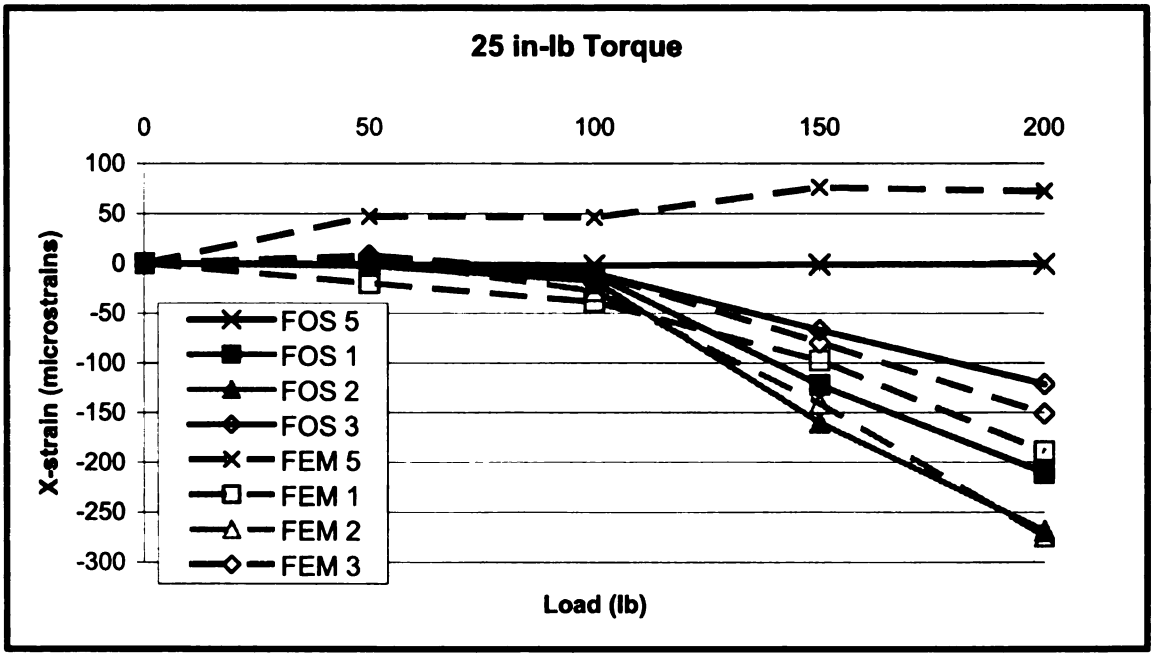

Figure 5.12 Results comparison for the Type 2 specimen: ε_{xx} for the 25lb-in bolt torque case.

The maximum strain in the bearing plane was recorded by FOS#2 and the value was -269με whereas the finite element analysis reported -274 με for the same point. The error between the finite element prediction and the experiment was approximately 2%.

An interesting observation for the *Type 2* specimen was that FOS#2 recorded higher strains than FOS#1. This was not observed with other specimens used in past research and initial finite element models were contradicting the experimental values. The reason for such results was assumed to be a small bulge on the inside of the hole close to the location of FOS#2. The pin connection case did not reveal such results and it was believed that the bulge was caused by the clamping force. The clamping force initiated a larger deformation amplified by either pockets of air trapped during the molding process or a matrix-rich area in the specimen. The bulge caused a shift in contact surface and an unexpected jump in strain for the plate regions monitored by FOS#2 and FOS#3.

Bearing damage of composite plates in single-lap bolted joints is commonly found on the edge of the hole. As the load increases, the bearing damage propagates further from the edge of the hole. This is consistent with the findings of McCarthy *et al.* (2002).

In a normal situation, and consistent with results obtained with *Type 1* specimens, the edge of the hole coincides with the first point of contact. In the case of an unforeseen matrix-rich area, air pocket or manufacturing defect that can create a bulge in hole wall, the bearing damage sustained by the composite plate is expected start at the location of the first point of contact, which is shifted. The shift may lead to different failure modes than expected. The assumed bulge was represented in the finite element model by a reduced regional bolt-hole clearance. The assumed bulge position and the finite element results are shown in Figure 5.13. Corrections to the finite element model to account for the bulge validated the assumed existence of a bulge in the hole wall.

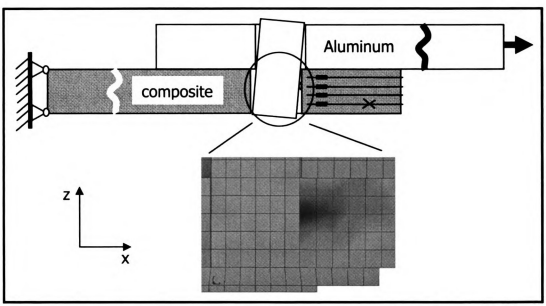

Figure 5.13 Type 2 specimen: Assumed bulge representation compared with FEA results.

The results show a reasonably good correlation between finite element analysis and experiments in the bearing region of the composite plate. On the opposite side of the hole, however, FOS#5 recorded very low strains during experiments. The finite element model showed tensile strains increasing immediately after load was applied on the joint. A possible cause would be the lack of a secondary contact point on the region monitored by FOS #5. The secondary contact point was missing because the bolt is constrained by the washer and clamping force.

The axial strains in the area around the fastener are shown in Figure 5.14. clearance is also visible as well as bending caused strains in the far-field region of the composite plate.

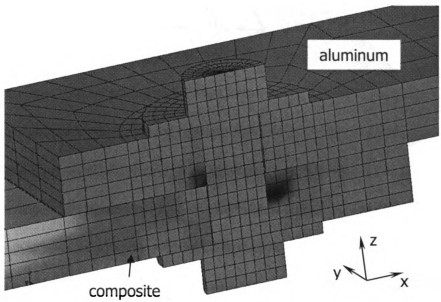

Figure 5.14 *Type 2* specimen: ε_{xx} strain map at 200lb load and 25lb-in bolt torque.

A closer view of the axial strain map of the composite plate, as shown in Figure 5.15, reveals the shifted contact point between the bolt shank and the composite plate. There is no secondary contact point visible. Tension strains on the side of the hole are also a bit shifted, most likely because of the change in contact patch location.

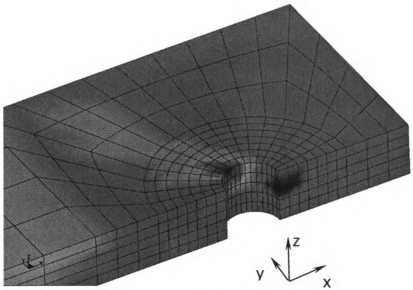

Figure 5.15 *Type 2* specimen: ε_{xx} strain map at 200lb load and 25lb-in bolt torque.

Chapter 6

CONCLUSIONS

This study was concerned with the evaluation of strain fields in thick composite plates used in single-lap bolted joints. The area of interest was the bearing plane region close to the bolt hole. Both experimental and finite element analyses were performed to better evaluate possible failure causes and three-dimensional effects present in thick composite bolted joints.

The materials used for the two plates forming the bolted joint were aluminum 2024-T4 and style 3733 E-glass/epoxy. The composite plate had 60 plies and 0.35 volume fraction. Macro-mechanical properties for the composite plate were taken from the literature and validated by experiments. The validation was performed against experimental data recorded with surface-mounted resistance strain gages and embedded fiber-optic strain gages.

Experimental data for the pin connection and the bolted joints were recorded by embedded fiber-optic strain gages and a through-the-hole type load

transducer. The fiber-optic strain gages were embedded in the bearing plane of the composite plate for both *Type 1* and *Type 2* specimens. For *Type 2* specimens one sensor was also placed inside the composite plate on the opposite side of the hole from the bearing plane. The numerical analysis was performed using both ANSYS and LS-DYNA commercially available finite element codes. Experimentally validated material properties were used for the composite plate. A comparison between finite element analysis and experiments was performed for each load case and specimen type. The finite element analysis correlated reasonably well with the experiments. Three-dimensional effects present in the single-lap bolted joints, such as secondary bending, were accurately determined.

A fiber-optic strain gage installation method and safety procedures were developed.

The maximum strains present in the bearing plane were experienced for the pin connection case. This case is analogous to a loose or missing nut in the bolted joint. In the 25-lb-in bolt torque case, the maximum recorded strains were significantly lower compared to the pin connection case. An optimum bolt torque value needs to be determined in future research.

Visco-elastic effects have a major influence on experimental results. Such effects were minimized during experiments by use of conical spring washers, torque application techniques and experiment procedures.

In the case of the pin connection the maximum strain resulting from the finite element analysis was -653 με while the experimental data at the same point showed -662 με. This corresponds to less than 1.5% difference between the finite element and the experiments.

For the 25lb-in case, the finite element analysis reported a maximum strain of -274 με in the bearing plane. The experimental data recorded for the same point showed a value of -269 με. The difference between the experiments and the finite element analysis was approximately 2%.

Type 2 specimen exhibited a different strain field in the bearing plane than *Type 1* specimens. The different behavior was assumed to be produced by a localized bulge in the hole wall. Finite Element Analysis models modified accordingly, to account for the localized bulge, successfully validated the assumption.

For both the pin connection and the 25lb-in bolt torque cases the maximum strains were successfully determined both experimentally and

numerically with the lower strains showing fairly good agreement between experimental and numerical analysis. Further investigations are necessary to accurately determine variable bolt-to-hole clearance effects, explore a wide range of bolt-torque cases with optimum bolt-torque values and visco-elastic effects. These effects are known to produce results scattering and have a negative impact on the service life of the composite bolted joint.

Chapter 7

ERROR SOURCES

Error sources in this study are found in experimental as well as numerical analyses. Sources of error are:

- fiber-optic strain gages,
- finite element modeling,
- composite material mechanical properties,
- friction coefficients.

7.1 FIBER-OPTIC STRAIN GAGE ERRORS

During fabrication, the fiber-optic strain gages, although small, can create a localized matrix-rich region between the immediately adjacent plies. The visco-elastic effects present in the matrix during loading are amplified in the matrix-rich region thus influencing results. A matrix-rich region around an embedded optical fiber is shown in Figure 7.1.

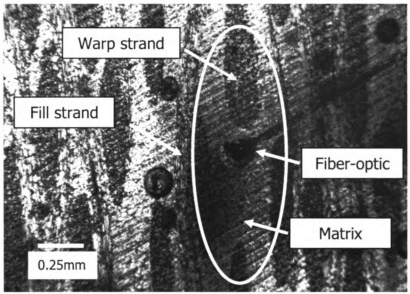

Figure 7.1 Fiber optic strain gage embedded in composite plate.

7.2 FINITE ELEMENT MODELING

Finite element errors influencing results are caused by material properties input, geometrical approximations, simplified fastener representation, friction coefficient and bolt-to-hole clearance values. Each probable cause has an influence on the results depending on the load case.

The simplified fastener approach, as shown in Figure 7.2, proved to be a good representation of the bolt assembly, but it does not account for washer-to-bolt head or washer-to-nut interactions. The impact of these interactions, along with washer-bolt clearance effects, needs to be further evaluated.

Figure 7.2 Simplified fastener finite element model.

7.3 MACRO-MECHANICAL PROPERTIES

Macro-mechanical properties of the E-glass/epoxy plate were taken from the literature and validated by experiments. The inherent errors of approximating the composite plate macro-mechanical properties from constituent material properties are therefore present.

The hand lay-up method used to fabricate the specimens creates the possibility for air-pockets within the composite plate. The particular epoxy used can dissipate air pockets quite efficiently. Nevertheless, some air pockets are still present and they are visible in Figure 7.1 as dark round spots.

7.4 FRICTION COEFFICIENTS

The values of the friction coefficients directly influence the FEA results. The largest surfaces coming in contact for the bolted joint and the pin connection were the overlapped plate surfaces. The friction coefficient between the composite and the aluminum had the biggest impact on the results. In the case of the *Type 2* specimen, a change in value from 0.45 to 0.48 in the composite-to-aluminum and composite-to steel friction coefficient resulted in a 20% reduction in maximum strain obtained with FEA for the FOS#2 position. Mold release, oxidation and other surface contaminants may produce wide variations in friction coefficients.

Chapter 8

FUTURE WORK

Taking into consideration the large spectrum of variables and parameters involved in studying single-lap single-bolt thick composite joints, more work is needed to fully characterize the behavior of such bolted joints. The following research directions should be considered in the future:

- Experimental and FE Analyses characterizing the use of conical spring washers in the bolted joint,
- Implementation of Bragg grating fiber-optic strain gages for far-field strains and structural health monitoring of such regions,
- Experimental determination of friction coefficients of composite joint parts,
- Optimization of the bolt torque value,
- Experimental and FE Analyses of strain reduction methods such as hole inserts,
- Experimental and FE Analyses of thicker sandwich-type composite materials in single-lap bolted joints.

APPENDIX 1

APPENDIX 1

Fabrication of E-glass/Epoxy Plate with Embedded Fiber Optic Sensors

OBJECTIVE

The objective of this research work was to analyze strains in the bearing plane of a "thick" composite plate in a single-lap bolted joint. The sensors used are non-compensating fiber-optic strain gages as manufactured by FISO Technologies. These sensors were embedded in the plate at the time of fabrication. The fabrication steps listed below can be used as guidelines for future specimen fabrication.

STEP 1

This step included the initial measurements, the manufacturing of the mold and the cutting of the E-glass weave to the preset dimensions.

Tools and materials:

- Calculator (optional)
- Marker
- Ruler
- Melamine sheet
- Card board (cellulose based)
- Circular saw
- Staple gun or solid stapler
- Silicone sealer or tacky tape
- Pair of clamps
- Protection glasses
- Protection breathing mask (for cutting E-glass weave and melamine)
- Scissors
- E-glass weave (for this experiment, E-glass style 3733 was used)

1. Initial measurements

The desired specimen dimensions, used in this research work, are shown in Figure A.1. Based on these dimensions, the size of the mold was set to be larger than the specimen. This allowed us to trim the edges in order to obtain consistent material properties throughout the plate because edges are particularly rich in matrix.

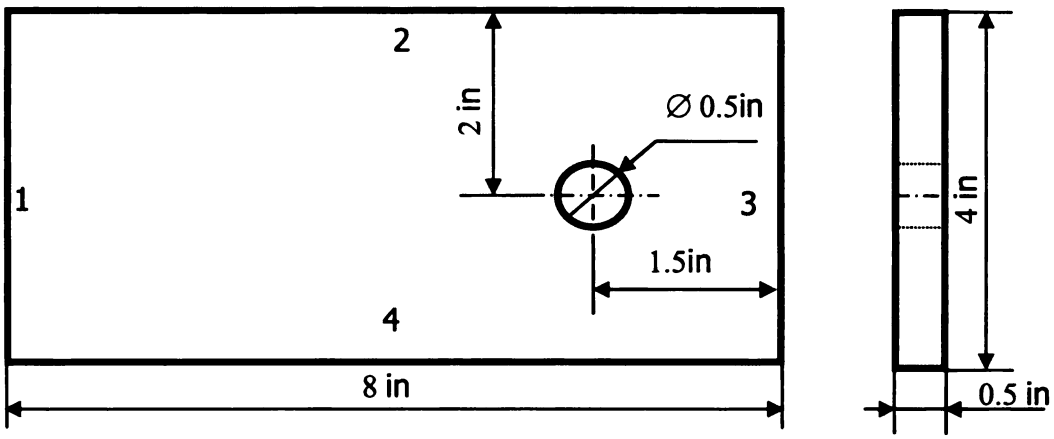

Figure A.1. Specimen dimensions.

The mold was done by cutting each side of the mold from a melamine sheet. The dimensions of the mold components are shown in Table A.1.

Table A.1. Mold dimensions.

No. of Pieces	Length (in)	Height (in)	Thickness (in)
1	10	5	3/4
1	5	2	3/4
2	10 3/4	2	3/4
1	9 5/8	4 5/8	3/4

After the components were cut to the preset dimensions, they were assembled with one handed bar clamps. Then they were joined together with staples. The small gaps at the joints were filled with tacky tape (silicone can be

used as well). Cardboard was used for the side of the mold where the bearing plane sensors were set to come out of the plate.

A sketch of the mold and a picture with the mold and the bar clamps can be seen in Figure A.2 and Figure A.3, respectively.

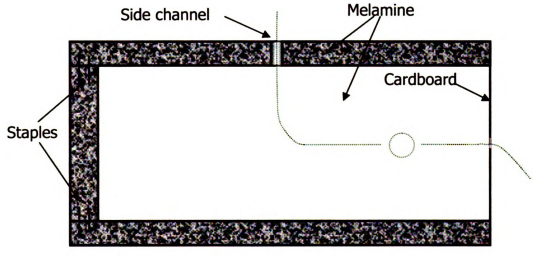

Figure A.2. Mold shape.

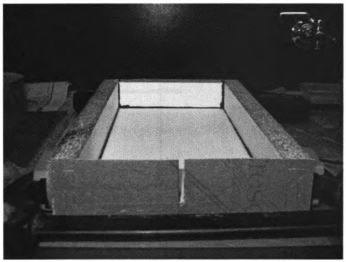

Figure A.3. The mold: before cutting the side channel to accommodate the side exiting sensor.

2. Sensor position

Specimen was set to have five fiber optic sensors embedded at fabrication time. Positioning the sensors required exact calculations so that the tip of the sensor was not to close to the hole wall. Figure A.4 shows the position of each fiber-optic sensor. The distance between each of the four sensors in the bearing plane is equal to 0.1in.

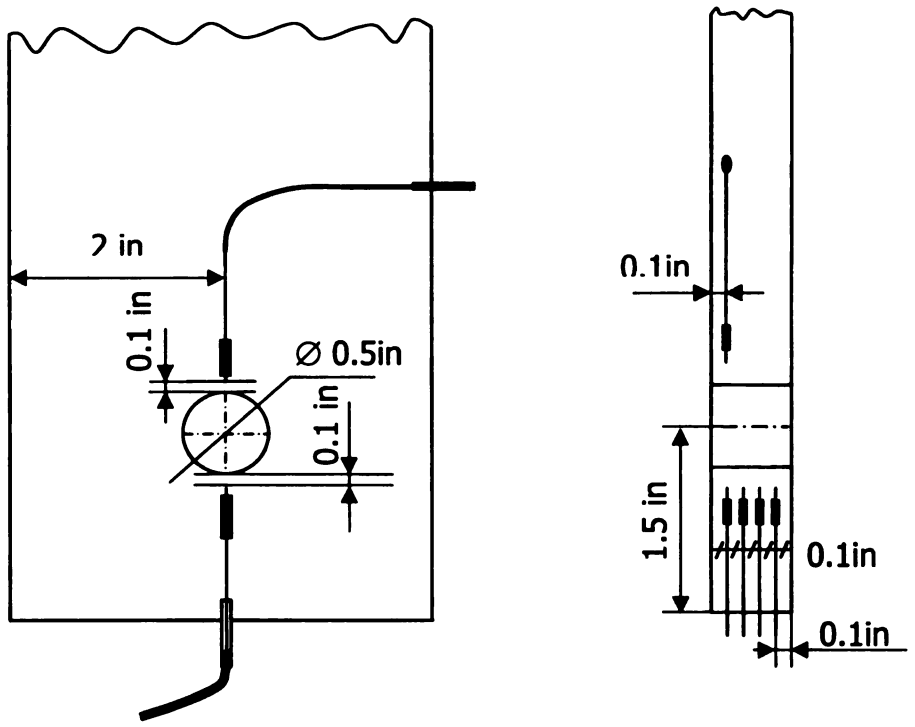

Figure A.4. Fiber-optic sensors positions.

Shrink wrap tubing was attached to the PVC coating of the fiber-optic sensors to protect the naked fibers that come out of the specimen.

STEP 2

Tools and materials:

- Fiber-optic sensors
- 1/16" heat-shrink tubing (or smaller diameter)
- Soldering iron or small heat gun

1. Attaching Shrink Wrap Tubing

The shrink wrap tubing was cut to 1 inch per segment. Each segment was then positioned such that it was overlapping the PVC jacket. The shrink wrap tubing was heated up by means of a soldering iron. The fiber and the shrink wrap were rotated above the soldering iron, ensuring that there was a small gap between the hot solder iron and the shrink wrap. Once this operation was completed, the shrink wrap needed repositioning due to axial shrinkage to ensure a proper placement with respect to the end of the fiber. One end of the tubing was overlapping and squeezing the PVC jacket (about 1/3in) and the other end had to be close enough to the tip of the sensor so that it would be fixed in the specimen during lay-up (about 1/8"). A sensor with the shrink wrap tubing attached to it is shown in Figure A.5.

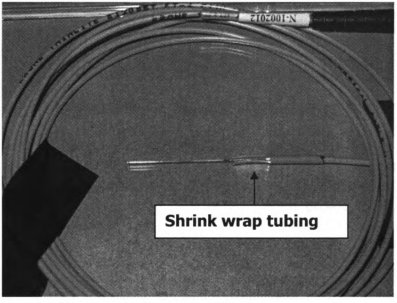

Figure A.5. Fiber optic sensor bearing shrink wrap tubing.

In order to maintain the position of the sensor during lay-up and curing processes, the fiber-optic sensors were attached to the fiber glass cloth. Each of the fiber-optic sensors was taped to a ruler for safety and positioning purposes. The ruler allowed for precise positioning of the tip of the sensor and also kept the fiber from moving.

STEP 3

Tools and materials:

- Previously cut E-glass weave
- One ruler for each gage

- Tape
- Erasers to hold the tip of each gage in place
- Epoxy or aluminum filled epoxy

Two small drops of DEVCON Aluminum Liquid (F-2) were used to attach each sensor to the fiber glass cloth. The sensors were positioned such that they would blend between two longitudinal E-glass fiber strands, as shown in Figure A.7 and Figure A.6.

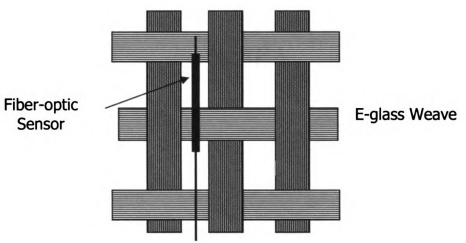

Figure A.6. Sensor position on the E-glass weave.

During this step the mold was coated with successive layers of mold release agent and let to dry as per manufacturer instructions.

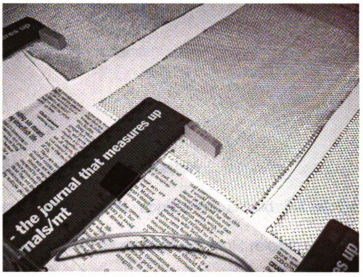

Figure A.7. Sensor positioning.

STEP 4

Tools and materials:

1. Latex gloves or similar
2. Mold release agent and applicator
3. Epoxy and hardener
4. E-glass with attached sensors
5. Mold
6. Small cups to temporarily store the epoxy and the curing agent
7. Weigh scale
8. Spoon or wood tongue depressor

9. Foam roller
10. Tray to wet the foam roller

1. **Mold Release Agent Application**

The mold release agent application should follow the manufacturer instructions closely. LOCTITE Frekote 55-NC mold release agent was used for the specimen. This mold release agent features a drying time of less than a minute.

The mold release was applied at room temperature by means of a small folded E-glass cloth (any lint free cloth can be used). Three successive base coats were applied at five minutes intervals followed by a final coat that was let to dry for thirty minutes before the lay-up process began.

2. **Epoxy and hardener mixing**

Once the epoxy is mixed together with the curing agent, the pot life does not allow a long lay-up period. It is practically impossible to lay-up all 60 layers in the pot life. Because of this fact, multiple pairs of small pots were used to temporarily hold epoxy and hardener separately. Pots forming a pair were weighed to fit manufacturer recommended mixing ratio. Each pair was then mixed as the need for more epoxy occurred during lay-up.

Optically clear epoxy 20-3302 as manufactured by Epoxies, Etc... was used, to be consistent with previous research.

3. Lay-up Process

Final position of the fiber-optic sensors on the vertical axis is directly influenced by the thickness of the plate. The number of layers was previously set to be 60. The number of fiber-optic sensors in the bearing plane was set to four. One sensor shared the same E-glass weave layer with the one on the opposite side of the hole. Every 12^{th} E-glass weave layer had a sensor (two for the layer bearing both bearing plane and opposite side sensors).

Before starting the lay-up, the surface of the mold was wet with epoxy using the roller. Then the first layer was laid in the mold and then pressed and wet with the roller. This procedure was repeated for each layer that did not contain any sensors. Special care was paid for the layers having sensors attached to them.

As a recommendation, any sensor bearing layer should have an extra layer laid on top before wetting. This prevents accidental damage to the sensors by pressing with the roller directly on the sensors.

STEP 5

This step involved removing the plate from the mold, drilling the hole and trimming the edges to the desired dimensions.

Tools and equipment:

- Flat tip screwdriver
- Special flat plate sharpened aluminum tool (explained below)
- Ruler
- Pencil
- Press drill
- Circular saw
- 1/4" diameter drill bit
- 15/32" diameter drill bit
- 31/64" diameter chucking reamer
- 1/2" diameter chucking reamer
- Thin blade hand saw
- Flat hand file
- Sand paper

Special tool

This tool is very useful for removing the mold parts that eventually stick to the composite plate after curing. It is very simple to do from a 1/8" thick aluminum sheet (or similar). It is bent at one end such that it forms an L-shape and it is sharpened at the other end by filing (or similar). Approximate dimensions for the tool used in the project are shown in Figure A.8.

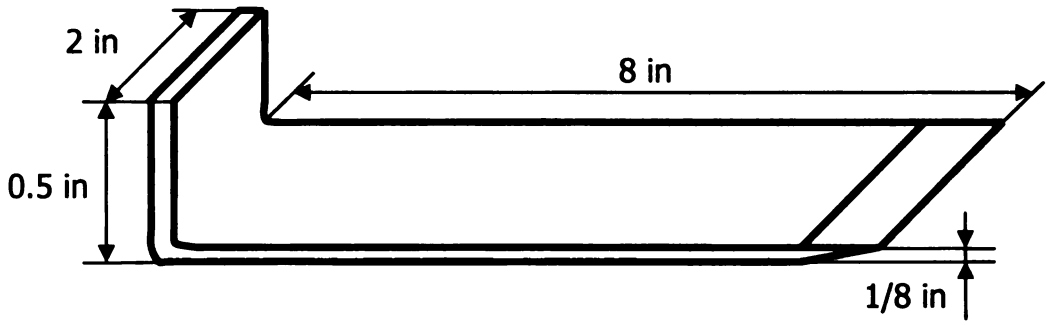

Figure A.8. Special tool for mold releasing.

1. Removing the plate from the mold

Parts of the mold that were sticking to the plate were removed using a combination of flat tip screwdriver and the special tool. The special tool is sharp enough to be inserted between the plate and the mold and then punched down until the plate separated from the mold.

2. Drill hole

The position of the hole needed to be calculated first. Special attention was devoted to ensure that any of the tools used to drill the hole would not come closer than expected to the sensor tips. Practice on a similar material as the specimen is recommended.

After the center of the hole was identified the plate was fixed to the workbench so that it would not move during the drilling process. Press drill rotational speed was set to 200rpm and small feed was used throughout the process. These steps were followed in the order listed below:

a. Drill hole with 1/4" drill bit
b. Enlarge hole with 15/32" drill bit
c. Reaming using 31/64" chucking reamer
d. Reaming using 1/2" chucking reamer

3. Trim edges

The cardboard was easily cut after the plate cured and the integrity of the sensors was preserved. The trimmed region is shown in Figure A.9. The other edges needed to be cut by means of circular saw and hand saw. The hand saw was used to precision cut the slack material close to the side exiting sensor. Filing and sanding were done as needed for a smooth finish.

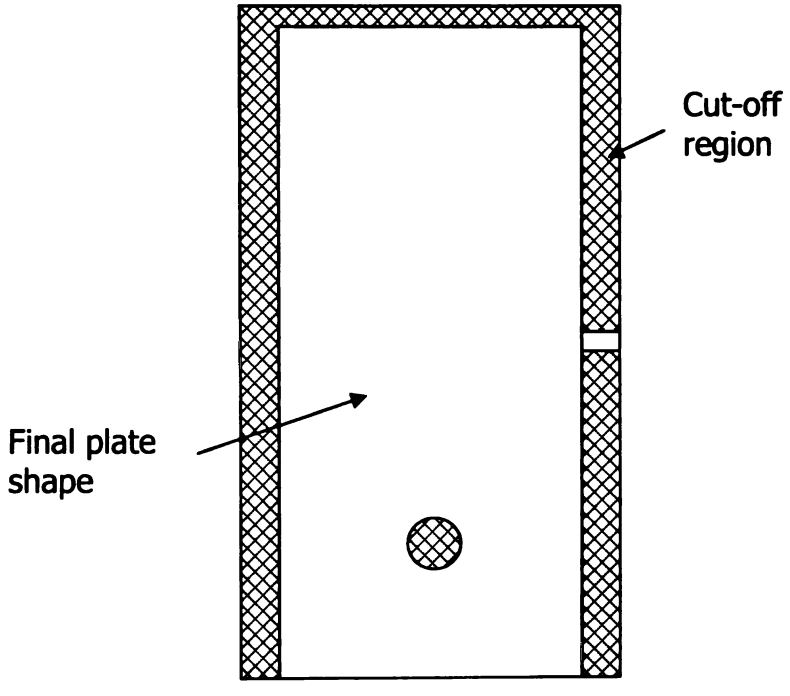

Figure A.9. Composite plate trimming.

REFERENCES

REFERENCES

ANSYS v8.0 Documentation - ANSYS Inc.,

Belleville, C. and G. Duplain (1993). Fabry-perot optical sensing device for measuring a physical parameter. U. S. Patent. **5,202,939**.

Belleville, C. and G. Duplain (1993). "White-light interferometric multimode fiber-optic strain sensor." OPTICS LETTERS **18**(1): 78-80.

Belleville, C. and G. Duplain (1995). Fabry-Perot optical sensing device for measuring a physical parameter. U. S. Patent. **5,392,117**.

Camanho, P. and F. Matthews (1997). "Stress analysis and strength prediction of mechanically fastened joints in FRP: A review." COMPOSITES PART A-APPLIED SCIENCE AND MANUFACTURING **28**(6): 529-547.

Chawla, K. K. (1998). Composite materials : science and engineering. New York, Springer.

Chen, W. H., S. S. Lee, et al. (1995). "3-Dimensional contact stress-analysis of a composite laminate with bolted joint." Composite Structures **30**(3): 287-297.

Chutima, S. and A. P. Blackie (1996). "Effect of pitch distance, row spacing, end distance and bolt diameter on multi-fastened composite joints." Composites Part A-Applied Science And Manufacturing **27**(2): 105-110.

Dasgupta, A., R. K. Agarwal, et al. (1996). "Three-dimensional modeling of woven-fabric composites for effective thermo-mechanical and thermal properties." COMPOSITES SCIENCE AND TECHNOLOGY **56**(3): 209-223.

Herakovich, C. T. (1998). Mechanics of fibrous composites. New York, John Wiley & Sons, Inc.

Herrera-Franco, P. J. and G. L. Cloud (1992). "Strain-relief inserts for composite fasteners - An experimental-study." Journal Of Composite Materials **26**(5): 751-768.

Hou, L. and D. S. Liu (2003). "Size effects and thickness constraints in composite joints." Journal Of Composite Materials **37**(21): 1921-1938.

Iancu, F., X. Ding, et al. (2004). Three-D photoelasticity, RSG, and finite element investigation of thick single lap bolted joints. SEM X International Congress & Exposition.

Ireman, T. (1998). "Three-dimensional stress analysis of bolted single-lap composite joints." Composite Structures **43**(3): 195-216.

Ireman, T., T. Ranvik, et al. (2000). "On damage development in mechanically fastened composite laminates." Composite Structures **49**(2): 151-171.

Kermanidis, T., G. Labelas, et al. (2000). Finite element modeling of damage accumulation in bolted composite joints under incremental tensile loading. European Congress on Computational Methods in Applied Sciences and Engineering.

Lawlor, V., M. McCarthy, et al. (2002). "Experimental study on effects of clearance on single bolt, single shear, composite bolted joints." PLASTICS RUBBER AND COMPOSITES **31**(9): 405-411.

McCarthy, M., V. Lawlor, et al. (2002). "Bolt-hole clearance effects and strength criteria in single-bolt, single-lap, composite bolted joints." COMPOSITES SCIENCE AND TECHNOLOGY **62**(10-11): 1415-1431.

Parmley, R. O. (1989). Standard hadbook of fastening & joining. New York, McGraw-Hill Publishing Company.

Starikov, R. and J. Schon (2002). "Experimental study on fatigue resistance of composite joints with protruding-head bolts." Composite Structures **55**(1): 1.

Tong, L. (2000). "Bearing failure of composite bolted joints with non-uniform bolt-to-washer clearance." Composites Part A: Applied Science and Manufacturing **31**(6): 609.

Whitney, T. J., E. V. Iarve, et al. (2004). "Singular stress fields near contact boundaries in a composite bolted joint." International Journal of Solids and Structures **41**(7): 1893.